Long Noncoding RNA *MIR4435-2HG* Suppresses Colorectal Cancer Initiation and Progression By Reprogramming Neutrophils

Hongfei Yu[1], Chaoyi Chen[1], Fengyan Han[1], Jinlong Tang[1], Mengli Deng[1], Yumiao Niu[1], Maode Lai[2,3,4,5], and Honghe Zhang[1,3,4]

ABSTRACT

MIR4435-2HG, also known as *LINC00978*, has previously been described as an oncogenic long noncoding RNA (lncRNA). However, we show here that *Mir4435-2hg* depletion promoted colorectal tumorigenesis and progression in *in vivo* models of colitis-associated colorectal cancer, spontaneous intestinal adenomatous polyposis, and subcutaneous tumors. Alteration of *MIR4435-2HG* in colorectal cancer cells did not change the potential for cell proliferation, migration, or invasion *in vitro*. RNAscope assays showed that most *MIR4435-2HG* was located in the tumor stroma, which caused high expression of *MIR4435-2HG* in colorectal cancer tumor tissue. Transcriptome analysis of colorectal cancer tissues from wild-type and *Mir4435-2hg*–deficient mice revealed *Mir4435-2hg* as a tumor suppressor gene that regulated the immune microenvironment. Loss of *Mir4435-2hg* led to a decline in neutrophils and elevation of polymorphonuclear myeloid-derived suppressor cells (PMN-MDSC). In tissue-specific *Mir4435-2hg* knockout mice, we confirmed that *Mir4435-2hg* depletion in neutrophils, but not in intestinal epithelial cells, promoted colorectal cancer progression. Mechanistically, *Mir4435-2hg* depletion enhanced the immunosuppressive ability of PMN-MDSCs by disturbing their fatty acid metabolism. These findings suggest that *MIR4435-2HG* is a tumor-suppressing lncRNA whose deficiency could increase tumor-infiltrating PMN-MDSCs and enhance the immunosuppressive potential of PMN-MDSCs to promote colorectal cancer development. This provides a theoretical basis for further illustrating the pathogenesis of colorectal cancer and a potential antitumor immunotherapy target.

Introduction

Long noncoding RNAs (lncRNA) are a class of over 200 nucleotide transcripts without protein-coding capacity (1). Various studies demonstrate the vital roles of lncRNAs in tumorigenesis, proliferation, metastasis, angiogenesis, and regulation of the immune microenvironment (2, 3). As the third leading cause of malignant cancer in the world (4), colorectal cancer is regulated at the initiation and progression stages by the aberrant expression and mutations of lncRNAs. Our previous studies demonstrate that *LINC01133* can inhibit colorectal cancer epithelial–mesenchymal transition and metastasis by interacting with Serine And Arginine Rich Splicing Factor 6 (SRSF6; ref. 5), and high expression of the lncRNA *CYTOR* in tumor cells drives colorectal cancer progression (6). We also found that another novel lncRNA, *MIR4435-2HG*, which is highly homologous to *CYTOR* (7), is upregulated in colorectal cancer tumor tissue. An increasing number of publications have since then reported *MIR4435-2HG* as an oncogene in multiple tumor types, such as lung cancer (8, 9), hepatocellular carcinoma (10, 11), gastric cancer (12), breast cancer (13, 14), prostate cancer (15, 16), and colorectal cancer (17–19). These results were derived from analyses of clinical tissue samples or public databases and gain- or loss-of-function assays in *in vitro* tumor cell lines, but the roles of *MIR4435-2HG* in the tumor stroma or microenvironment, and its detailed regulatory mechanisms, remain unknown.

Myeloid-derived suppressor cells (MDSC) are a heterogeneous population of cells, including pathologically activated monocytes and relatively immature neutrophils, that are generated from many pathological conditions, such as infection, inflammation, and cancer. MDSCs consist of polymorphonuclear MDSCs (PMN-MDSC) and monocyte MDSCs (M-MDSCs), whose morphology and phenotype are similar to those of neutrophils and monocytes, respectively (20, 21). PMN-MDSCs are the prevalent population of MDSCs in most types of cancer, including lung, breast, colon, and pancreatic cancer (22, 23). The salient feature of MDSCs is their inhibition of T-cell proliferation and activation by inducing arginase-1 (Arg1), reactive oxygen species production, and nitric oxide production, which culminate in the promotion of tumor progression (24, 25). MDSCs have also been reported to produce prostaglandin E2, calcium-binding proteins S100A8/S100A9, matrix metalloproteinases, IL10, TGFβ, and other cytokines to promote angiogenesis, tumor proliferation, and metastasis (26). Clinical investigation has shown that the accumulation of

[1]Department of Pathology and Women's Hospital, Zhejiang University School of Medicine, Research Unit of Intelligence Classification of Tumor Pathology and Precision Therapy, Chinese Academy of Medical Sciences (2019RU042), Hangzhou, China. [2]Department of Pathology, Research Unit of Intelligence Classification of Tumor Pathology and Precision Therapy of Chinese Academy of Medical Sciences (2019RU042), Zhejiang University School of Medicine, Hangzhou, China. [3]Key Laboratory of Disease Proteomics of Zhejiang Province, Hangzhou, China. [4]Cancer Center, Zhejiang University, Hangzhou, China. [5]Department of Pharmacology, China Pharmaceutical University, Nanjing, China.

H. Yu, C. Chen, and F. Han contributed equally to this article.

Corresponding Authors: Honghe Zhang, Department of Pathology, Research Unit of Intelligence Classification of Tumor Pathology and Precision Therapy of Chinese Academy of Medical Sciences (2019RU042), Zhejiang University School of Medicine, Yuhangtang Road 866#, Hangzhou, Zhejiang 310058, China. E-mails: honghezhang@zju.edu.cn; and Maode Lai, lmp@zju.edu.cn

Cancer Immunol Res 2022;10:1095–110

doi: 10.1158/2326-6066.CIR-21-1011

MDSCs positively associates with advanced cancer stage and metastatic burden in patients with colorectal cancer (27, 28).

So far, some lncRNAs, such as *PVT1* (29), *lnc-C/EBPβ* (30), and *lnc-chop* (31), have been identified to regulate the immunosuppressive activity of MDSCs. However, the roles of lncRNAs in MDSCs have still not been clarified in detail. In this study, our findings repositioned *MIR4435-2HG* as a tumor-suppressing lncRNA in colorectal cancer. *Mir4435-2hg* depletion increased tumor-infiltrating PMN-MDSCs and promoted lipid accumulation in MDSCs, thus enhancing the immunosuppressive function of MDSCs and promoting tumorigenesis and progression in both colitis-associated and $Apc^{min/+}$ spontaneous colorectal cancer mouse models. These findings imply that we need to reexamine the conclusions drawn from previous *MIR4435-2HG* expression data and experiments *in vitro*.

Materials and Methods

Cell lines and culture

Colorectal cancer cell lines DLD1, HCT8, HT29, HCT116, RKO, SW480, SW620, and CT26 were purchased from the ATCC in 2011. The MC38 cell line was kindly provided by Cell Bank/Stem Cell Bank, Chinese Academy of Sciences (Shanghai, China) in 2015. DLD1, HCT8, HCT116, HT29, SW480, SW620, CT26 cells were cultured in RPMI1640 (Gibco) and RKO, MC38 cells were cultured in DMEM (Gibco) medium according to the manufacturer's instruction, with 10% FBS (Gibco) and 1% penicillin–streptomycin (Biosharp, catalog no. BL505A) in a humidified atmosphere at 37°C with 5% CO_2. All cells were frozen at passages 2 to 5 after purchase. Experiments were performed using passages 3 to 20 after removal from liquid nitrogen. Mycoplasma was test routinely using GMyc-PCR Mycoplasma Detector Kit (Yeasen). The most recent cell line authentication was in September 2018 by short tandem repeat (STR) analysis in Forensic Science Center, Zhejiang University, Hangzhou, China.

Transfection of vectors and siRNA

For overexpressing *MIR4435-2HG* in DLD1 and HCT116 or *Mir4435-2hg* in MC38 and CT26 cells, plasmids containing *MIR4435-2HG* (NR_015395.2) or *Mir4435-2hg* variant 1 (NR_028589.1), variant 2 (NR_028590.1), variant 3 (NR_028591.1), respectively, were constructed on the basis of pCDH empty backbone (WZ Biosciences Inc.) using ClonExpress II One Step Cloning Kit (Vazyme, catalog no. C112). pCDH empty vector was used as control. Plasmids were then transfected into DLD1, HCT116, MC38 or CT26 by lipo2000 (Invitrogen, catalog no. 11668019) according to the manufacturer's instructions. siRNAs targeting *MIR4435-2HG* (synthesized in Gemma, Supplementary Table S1) were transfected into SW480 and RKO cells using the Genmute siRNA transfection reagent (SignaGen, catalog no. SL100568) according to the manufacturer's instructions. The overexpressing or silencing effects were confirmed by RNA isolation and quantitative PCR, as detailed below.

Construction of knockout cell lines via CRISPR/Cas9

To construct *MIR4435-2HG*-deficient SW480 cells and *Mir4435-2hg*–deficient MC38 cells, 2 μg pSpCas9-BB-2A-GFP plasmid containing two sgRNAs (purchased from Genscript; sgRNA sequences are listed in Supplementary Table S1) were transfected to cells at 50% confluence in a 6-well plate by Lipofectamine 2000 according to the manufacturer's instructions. After one week, single GFP^+ cells were selected by Beckman moflo Astrios EQ into wells of a 96-well plate. These single-cell clones were cultured as detailed above, and knockout was confirmed by PCR and RT-qPCR at the genome and transcriptional level. The clones without editing by Cas9 were used as mock cells. sgRNA sequences and PCR primers are listed in Supplementary Table S1.

Mice and colorectal cancer tumor models

$Mir4435\text{-}2hg^{+/-}$, $Mir445\text{-}2hg^{flox/+}$, Villin-Cre, S100a8-Cre mice were constructed through CRISPR/Cas9 and pronuclear microinjection techniques by GemPharmatech Co., Ltd, as indicated in Supplementary Figures. $Apc^{min/+}$ mice were a gift from Dr. Rongpan Bai, Zhejiang University School of Medicine. Primer sequences for PCR genotyping are listed in Supplementary Table S1. All mice were C57BL/6J background which were bred and maintained under pathogen-free conditions at the laboratory animal center, Zhejiang University. All mice were monitored every day by the staffs of the laboratory animal center and twice one week by the authors. The protocol (ZJU20160023) for this study was approved by the Institutional Animal Care and Use Committee at Zhejiang University.

For the azoxymethane (AOM)/dextran sulfate sodium (DSS)-induced colorectal cancer model, 6-week male wild-type (WT), $Mir4435\text{-}2hg^{-/-}$, $Mir445\text{-}2hg^{flox/flox}$, $Mir445\text{-}2hg^{flox/flox}$ Villin-Cre, $Mir445\text{-}2hg^{flox/flox}$ S100A8-Cre mice were injected intraperitoneally with 10 mg/kg AOM (Sigma-Aldrich, catalog no. A5486), and after one week, they were fed on and off 1.5% DSS (MPbio, catalog no. 160110) in the drinking water. One week of 1.5% DSS in the drinking water, followed 2 weeks of normal water constituted one DSS cycle. As indicated figures, mice were euthanized after two DSS cycles for the short-term cohort or after three DSS cycles for the classical term cohort. For the long-term cohort, mice were fed with normal water for another 15 weeks after three DSS cycles before euthanasia. In the cohort for survival analysis, mice were fed with normal water after three DSS cycles until death. The colon was harvested, cut open along the main axis, washed with saline, and tumor numbers were counted. Tumor size was defined as the tumor diameter measured by a caliper, and tumor burden was defined as the summation of total tumor volume. Histologic examination was performed on paraffin-embedded sections after hematoxylin and eosin (H&E) staining, as detailed below.

For spontaneous intestinal adenomatous polyposis, $Apc^{min/+}$ mice were sacrificed at 4 months old. Small intestines and colons were longitudinally cut open to count tumor numbers. Histologic examination was performed on paraffin-embedded sections after H&E staining, as described below.

For subcutaneous tumor models, male WT, $Mir4435\text{-}2hg^{-/-}$, $Mir445\text{-}2hg^{flox/flox}$, $Mir445\text{-}2hg^{flox/flox}$ S100A8-Cre mice aged 6–8 weeks were subcutaneously injected in the right flank with 1×10^5 WT MC38 cells. For Supplementary Fig. S5D, 1×10^6, 1×10^4, or 2×10^3 WT MC38 cell were injected as indicated in the figure. In **Fig. 2H**, 1×10^5 mock or KO MC38 cells were injected as indicted in the figure. Tumor length and width were measured with a Vernier caliper every three days. Tumor volume was calculated as length × $\text{width}^2/2$.

For verifying tissue-specific depletion of *Mir4435-2hg*, neutrophils and intestinal epithelial cells were collected from naïve $Mir445\text{-}2hg^{flox/flox}$, $Mir445\text{-}2hg^{flox/flox}$ Villin-Cre and $Mir445\text{-}2hg^{flox/flox}$ S100A8-Cre mice. Neutrophils were collected from bone marrow (as described below) by flow cell sorter (Beckman moflo Astrios EQ) as labeled $CD11b^+Ly6G^+$ cells (antibodies list in Supplementary Table S2). Intestinal epithelial cells were

collected by digesting colons using striping buffer containing 5 mmol/L EDTA (Invitrogen, catalog no. AM9260G), 1 mmol/L DTT (Beyotime, catalog no. ST041), 5% FBS in HBSS (Beyotime, catalog no. C0219), in 37°C 150 rpm for 40 minutes in the MQW-63R shaker. RNA isolation and quantitative PCR were then carried out as detailed below to verify the *Mir4435-2hg* depletion.

H&E staining

Brain, heart, kidney, liver, lung, spleen, stomach, small intestine, colon tissues from naïve 8-week male WT and *Mir4435-2hg*$^{-/-}$ mice, colon tissues from AOM/DSS-induced colorectal cancer models, and small intestine and colon tissues from 4-month *Apc*$^{min/+}$ mice were fixed with 10% neutral buffered formalin and paraffin embedded. After being sectioned, deparaffinized, and rehydrated, 4-μm-thick sections were stained with hematoxylin (Sigma-Aldrich, catalog no. H9627) for 10 minutes and eosin (Sigma-Aldrich, catalog no. 230251) for 2 seconds at room temperature. The slides were scanned using the NanoZoomer digital slice scanner (Hamamatsu). Tissue alterations were determined via tissue morphology, structure and cell morphology by a pathologist.

IHC

Four-micron-thick paraffin-embedded colon sections from the AOM/DSS-induced colorectal cancer models were deparaffinized in xylene (Sinopharm) and rehydrated through a graded series of ethanol solutions (Sinopharm). After blocking endogenous peroxidase activity in 3% hydrogen peroxide (ZSGB-BIO) at room temperature for 15 minutes, the tissue sections were treated with 0.01 mol/L citrate buffer (pH 6.0; OriGene) under high pressure in a pressure cooker for 3 minutes to complete antigen retrieval. Blocking was performed with 10% bovine serum (Gibco) for 30 minutes at room temperature, and then the sections were incubated with primary antibodies to CD8a (1:500) and MRP8 (1:1,000) overnight at 4°C (Supplementary Table S2), followed by incubation with 100 μL goat anti-rabbit secondary antibody (ZSGB-BIO, catalog no. PV6001) at room temperature for 30 minutes. Staining was visualized with 3,3′-diaminobenzidine (DAB) (ZSGB-BIO, catalog no. PV8000), and sections were counterstained with hematoxylin, dehydrated, and covered with a coverslip. The slides were scanned using the NanoZoomer digital slice scanner (Hamamatsu). Image analysis and quantitation were performed with ImageJ (NIH, Bethesda, MD).

Splenocytes and MC38 cell coculture assays

WT MC38 cells in logarithmic phase were trypsinized, washed twice to remove residual FBS, and then stained with 5 μmol/L CFSE (eBioscience, Cat# 65–0850) at room temperature for 10 minutes. Labeling was stopped by adding 4 to 5 volumes of cold 1640 medium containing 10% FBS, and then cells were incubated on ice for 5 minutes. After washing three times with complete medium, 2×10^5 CFSE-labeled MC38 cells were plated in 12-well plates with splenocytes isolated WT or *Mir4435-2hg*$^{-/-}$ mice after erythrocytes were lysed using RBC Lysis Buffer (Santa Cruz Biotechnology, catalog no. sc-296258). After incubating for 40 hours, both splenocytes and tumor cells were collected for flow cytometry analysis, as described below.

Bone marrow–derived MDSCs

Tibias and femurs from WT and *Mir4435-2hg*$^{-/-}$ mice were removed, and bone marrow (BM) cells were flushed from the bones in PBS containing 5% FBS. Erythrocytes were removed using RBC Lysis Buffer. A total of 1×10^6/mL BM cells were plated in 6-well plates in RPMI1640 complete medium containing 10% FBS, 1% penicillin–streptomycin, and 20 ng/mL GM-CSF (BioLegend, catalog no. 576304). 25% (v/v) MC38/CT26 tumor cell culture medium was added as required, which was prefiltered using 0.22-μm filters (Millipore). After 3 days, BM-derived MDSCs were collected for flow cytometry analysis, RNA isolation, and suppressive function assays, as detailed below.

Flow cytometry analysis

Cells used for flow cytometry analysis were isolated from the indicated tissues. Peripheral blood was collected from the retro-orbital plexus or submandibular vein plexus. Splenocytes were collected by dissociating the spleens with sterile forces and passing through a 40-μm cell strainer (Biosharp). BM cells were collected from tibias and femurs as described above. Erythrocytes in samples were lysed using RBC Lysis Buffer. Tumor tissues from mice were cut into small pieces and digested in RPMI1640 medium supplemented with 5% FBS, 1 mg/mL collagenase IV (Sigma-Aldrich, catalog no. C5138), 20 μg/mL hyaluronidase (Solarbio, catalog no. H8030) for 2 hours at 37°C in a shaker. Single-cell suspensions were obtained by passing through a 40-μm nylon cell strainer. Single-cell suspensions were first stained with Fc block (Biolegend, catalog no. 101320) and then treated with the indicated antibodies for 30 minutes in 4°C in the dark. All antibodies used are listed in Supplementary Table S2. 7-AAD (BD Biosciences, catalog no. 559925) was used to exclude dead cells. For intracellular staining, the Fix & Perm Kit (Multi Science, catalog no. GAS005) was used following the manufacturer's instructions. For lipid staining after surface staining, cells were resuspended in 500 μL of BODIPY 493/503 (Invitrogen, catalog no. D3922) at 1 μg/mL for 20 minutes at room temperature in the dark, and then washed three times with PBS. For reactive oxygen species (ROS) analysis, surface-stained cells were incubated with 10 μmol/L DCFH-DA probe (Beyotime, catalog no. S0033S) for 20 minutes at 37°C, and then washed three times with PBS before detection. Cells were run on Beckman CytoFLEX LX, and the data were analyzed by FlowJo 10.4 (Tristar).

RNA isolation and qPCR

Total RNA from cells or mouse colon tissues were isolated using TRIzol reagent (Invitrogen, catalog no. 15596018). Mouse colon tissues were homogenized by grinding in liquid nitrogen. For nuclear and cytoplasmic RNA fractionation, the PARIS Kit (Ambion, catalog no. AM1921) was used according to the manufacturer's instruction. cDNA was synthesized by HiScript II Reverse Transcriptase (Vazyme, catalog no. R223–01) and quantitative PCR analysis was performed by SYBR qPCR Master Mix (Vazyme, catalog no. Q711–02) according to the manufacturer's instruction in LightCycler 480 (Roche). *GAPDH* was detected in each experimental sample for normalization. Fold-change was calculated using the $2^{-\Delta\Delta C_t}$ method. Three independent experiments were performed in triplicate. Genes and primers are listed in Supplementary Table S1.

Cell proliferation, migration, and invasion assay

Cell proliferation was measured by CCK8 reagent (Boster, catalog no.AR1160) according to the manufacturer's instructions. Briefly, 2,000 cells were seeded in 96-well plates and incubated with 100 μL culture medium. An aliquot of 10 μL CCK8 was added and incubated for 2 hours. The absorbance at 450 nm was measured to calculate the

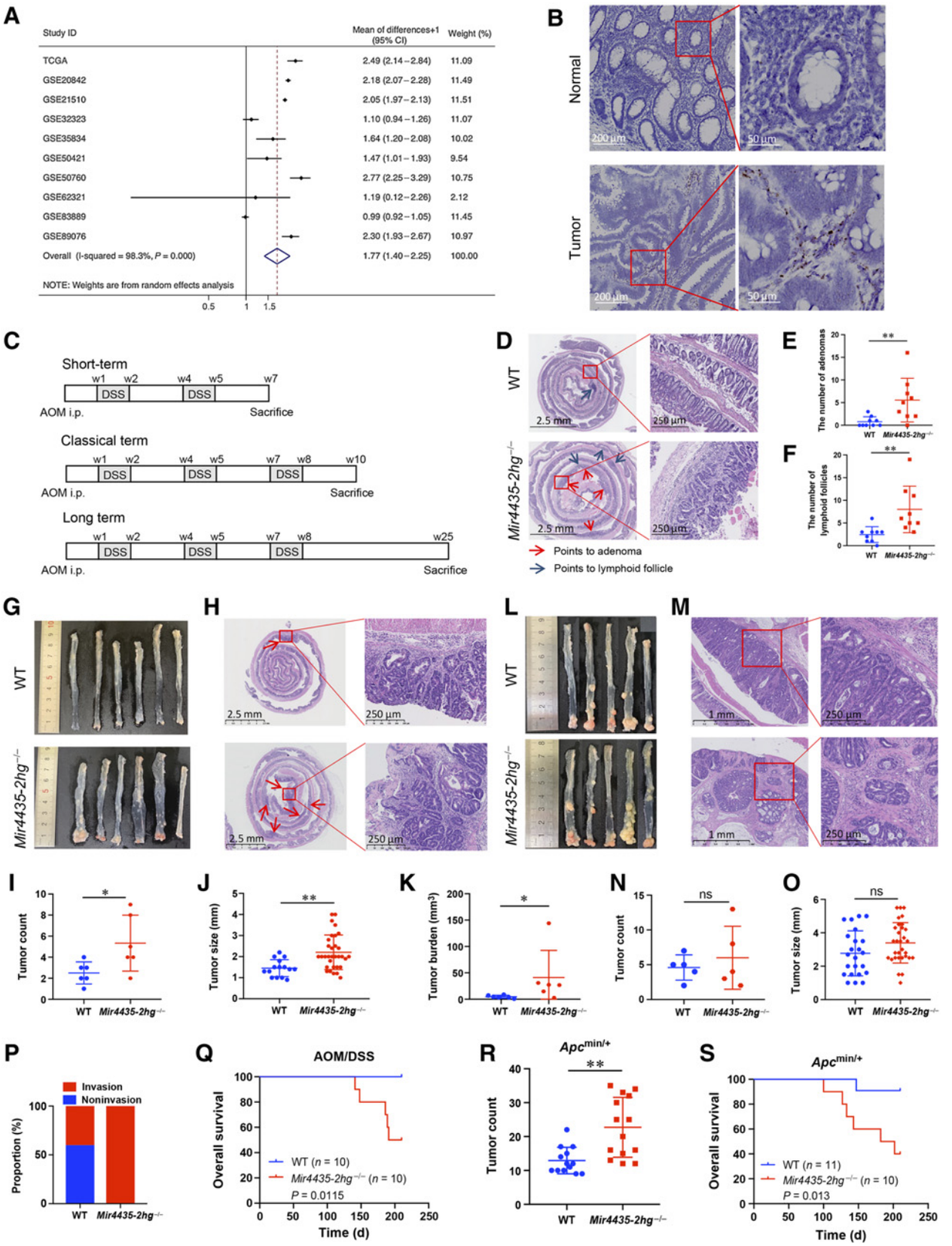
A
Study ID
Mean of differences+1 (95% CI)
Weight (%)
TCGA 2.49 (2.14 – 2.84) 11.09
GSE20842 2.18 (2.07 – 2.28) 11.49
GSE21510 2.05 (1.97 – 2.13) 11.51
GSE32323 1.10 (0.94 – 1.26) 11.07
GSE35834 1.64 (1.20 – 2.08) 10.02
GSE50421 1.47 (1.01 – 1.93) 9.54
GSE50760 2.77 (2.25 – 3.29) 10.75
GSE62321 1.19 (0.12 – 2.26) 2.12
GSE83889 0.99 (0.92 – 1.05) 11.45
GSE89076 2.30 (1.93 – 2.67) 10.97
Overall (I-squared = 98.3%, P = 0.000) 1.77 (1.40 – 2.25) 100.00
NOTE: Weights are from random effects analysis
0.5
1
1.5
B
Normal
Tumor
200 μm
50 μm
C
Short-term
w1 w2 w4 w5 w7
DSS
AOM i.p.
Sacrifice
Classical term
w1 w2 w4 w5 w7 w8 w10
Long term
w1 w2 w4 w5 w7 w8 w25
D
WT
Mir4435-2hg−/−
2.5 mm
250 μm
Points to adenoma
Points to lymphoid follicle
E
The number of adenomas
F
The number of lymphoid follicles
WT
Mir4435-2hg−/−
G
H
L
M
1 mm
I
Tumor count
J
Tumor size (mm)
K
Tumor burden (mm³)
N
ns
O
P
Invasion
Noninvasion
Proportion (%)
Q
AOM/DSS
Overall survival
WT (n = 10)
Mir4435-2hg−/− (n = 10)
P = 0.0115
Time (d)
R
Apcmin/+
S
WT (n = 11)
P = 0.013

numbers of viable cells. Migration and invasion assays were performed with transwell and Matrigel chamber plates (24-well format; 8-μm pore size; Corning Costar, catalog no. 3422) as described previously (32). ImageJ software was used to measure the cell area in the bottom chamber to quantify the cells that migrated across the filter. Each measurement was performed in triplicate, and the experiments were repeated three times.

Suppressive function assay

Splenocytes were isolated from spleens of wild-type C57BL/6 mice, and erythrocytes were lysed by RBC Lysis Buffer. Splenocytes were stained with 5 μmol/L CFSE (eBioscience, catalog no. 65–0850), and then 3×10^5 CFSE-labeled splenocytes were cocultured with 3×10^4 WT or *Mir4435-2hg*$^{-/-}$ MDSCs in a round-bottom 96-well plate precoated with 5 μg/mL anti-CD3 (eBioscience, catalog no. 14–0031) and 5 μg/mL anti-CD28 (eBioscience, catalog no. 14–0281) at 4°C overnight. After coculturing for 72 hours, T-cell proliferation was assessed by CFSE dilution using Beckman CytoFLEX LX, and data were analyzed in FlowJo 10.4.

GEO and TCGA databases analysis

The Gene Expression Omnibus (GEO) databases were systematically and comprehensively searched (up to October 16, 2017). The search details were '(colorectal [All Fields] AND (adenoma [MeSH Terms] OR adenoma [All Fields]) AND 9[n_samples]:1000[n_samples]) AND "Homo sapiens"'. The inclusion criteria were as follows: (i) datasets had paired clinical sample tissues; (ii) experiment type was expression profiling. The exclusion criteria were as follows: (i) spotted cDNA (two-channel ratio data) array; (ii) patient had antitumor treatments. All available data were included in processing and analysis. The selected gene expression data were downloaded from the GEO database in SOFT format. The SOFT files were reformatted to a table separate expression matrix using a custom C script (https://github.com/wenjie1991/GEO_parser). The expression data were annotated by the gene information from NCBI (ftp://ftp.ncbi.nlm.nih.gov/gene/DATA/GENE_INFO/Mammalia/Homo_sapiens.gene_info.gz). The Cancer Genome Atlas (TCGA) colorectal cancer dataset was downloaded from UCSC Xena (https://xenabrowser.net/). ESTIMATE (Estimation of STromal and Immune cells in MAlignant Tumor tissues using Expression data; ref. 33) R package was used to calculate the immune score in R software.

Colorectal cancer patient samples

Five colorectal cancer patient samples were used in the RNAscope assay, which were obtained from Sir Run Run Shaw Hospital, Zhejiang University in 2019 after informed consent by patients. The samples were formalin-fixed immediately after removal from patients and then dehydrated and paraffin-embedded. The collection and use of patient samples were approved by the Ethics Committee of department of Medicine, Zhejiang University (2016007).

RNAscope assay

The probe for *MIR4435-2HG* was synthesized by Advanced Cell Diagnostics (ACD lnc.). Detection of *MIR4435-2HG* in formalin-fixed paraffin-embedded (FFPE) human colorectal cancer tissues was performed using the RNAscope 2.0 HD Reagent Kit-Brown (ACD, catalog no. 322310) following the manufacturer's instructions. Briefly, 4-μm FFPE sections were deparaffinized, boiled with target retrieval reagent for 15 minutes, and then digested by protease at 40°C for 30 minutes, followed by hybridization for 2 hours at 40°C with Probe-*MIR4435-2HG*. After six steps of amplification, the probe was visualized with DAB, and cell nuclei were counterstained with hematoxylin. The slides were evaluated according to manufacturer's instructions by a pathologist.

RNA-sequencing, gene ontology functional analysis, and gene set enrichment analysis

RNA of colorectal tumor tissues from WT and *Mir4435-2hg*$^{-/-}$ long-term AOM/DSS mice, 4-month *Apc*$^{Min/+}$/WT, *Apc*$^{Min/+}$/*Mir4435-2hg*$^{-/-}$ mice, and neutrophils from bone marrow of 8-week WT and *Mir4435-2hg*$^{-/-}$ mice were extracted, sequenced, and analyzed by Bioacme. The tumor tissues were stored in RNA Keeper (Vazyme, catalog no.R501) and neutrophils were stored in TRIzol in −80°C and then shipped under the protection of dry ice. Three biological replicates were used. Gene differential expression analysis was performed using the Cuffdiff program in Cufflinks package (https://github.com/cole-trapnell-lab/cufflinks) (34). The Benjamini–Hochberg false discovery rate method was applied to correct for multiple hypothesis testing. The genes with adjust $P < 0.05$, fold change > 1.5 or < 0.67 were defined as differentially expressed genes and were candidates for further analysis. A gene expression heatmap was generated with Heatmapper (http://www.heatmapper.ca/). Gene ontology enrichment analysis was performed using the online tool DAVID (https://david.ncifcrf.gov/). The results were visualized using the R package ggplot2 in R software. Gene set enrichment analysis (GSEA) was applied to the H (hallmark) gene sets. The gene set collection database MSigDBv7.2 (http://www.gsea-msigdb.org/gsea/downloads_archive.jsp) was used and sets with size of 15 to 500 were selected. Permutation of genes was used to generate null distribution, and all other parameters were kept as default.

Figure 1.

Mir4435-2hg deletion promotes colorectal tumorigenesis and progression. **A,** Meta-analysis for the expression of *MIR4435-2HG* in colorectal cancer tumor tissues compared to paired adjacent normal tissues for 10 datasets from TCGA and GEO. **B,** RNAscope assay for detecting the sublocation of *MIR4435-2HG* in human colorectal cancer tissues. Brown dots represent *MIR4435-2HG* (data representative of $n = 5$). Scale bar, 200 μm; zoomed, 50 μm. **C,** Schematic of three cohorts of AOM/DSS-induced colorectal cancer using wild-type (WT) and *Mir4435-2hg*$^{-/-}$ mice. W, week; i.p., intraperitoneal injection. **D,** Representative H&E staining of colorectum from WT and *Mir4435-2hg*$^{-/-}$ mice in the short-term AOM/DSS model. Scale bar, 2.5 mm; zoomed, 250 μm. Quantification of adenomas (**E**) and lymphoid follicles (**F**) in the colorectum, counted from three different H&E staining sections of one sample. Each spot represents one mouse, $n = 9$/group. Gross view (**G**) and representative H&E staining (**H**) of colorectum from WT and *Mir4435-2hg*$^{-/-}$ mice in the classical term AOM/DSS model, $n = 6$/group. Scale bar, 2.5 mm; zoomed, 250 μm. Quantification of colon tumor number (**I**), tumor size (**J**), and tumor burden (**K**). For **I** and **K**, each spot represents one mouse. For **J**, each spot represents one tumor. Gross view (**L**) and representative H&E staining (**M**) of colorectum from WT and *Mir4435-2hg*$^{-/-}$ mice in long-term AOM/DSS model, $n = 5$ for each group. Scale bar, 1 mm; zoomed, 250 μm. **N,** Quantification of colon tumor number. Each spot represents one mouse. **O,** Quantification of tumor size. Each spot represents one tumor. **P,** Percentage of mice with invasive adenocarcinomas in long-term AOM/DSS model. **Q,** Survival analysis of WT and *Mir4435-2hg*$^{-/-}$ mice with AOM/DSS treatment, $n = 10$ per group. **R,** Quantification of tumor number from intestine and colorectum of 4-month *Apc*$^{Min/+}$/WT and *Apc*$^{Min/+}$/ *Mir4435-2hg*$^{-/-}$ mice. Each spot represents one mouse, $n = 13$–14/group. **S,** Survival analysis of *Apc*$^{Min/+}$/WT and *Apc*$^{Min/+}$/ *Mir4435-2hg* $^{-/-}$ mice, $n = 10$–11/group. Data are presented as mean±SD; statistical significance was assessed by an unpaired *t* test (**E**, **F**, **I**, **J**, **K**, **N**, **O**, **R**) or log-rank test (**Q** and **S**; ns, $P > 0.05$; *, $P < 0.05$; **, $P < 0.01$).

Statistical analysis

A two-tailed Student *t* test was used to test for significant differences between two groups in GraphPad v6.0 (GraphPad Software) or SPSS v23 (SPSS Inc.). Kaplan–Meier survival analysis was performed using the software IBM SPSS Statistics v23 with the Log-rank (Mantel–Cox) test. Data in this article are presented as mean ± SD. P-value <0.05 was considered statistically significant (*, $P < 0.05$; **, $P < 0.01$; ***, $P < 0.001$; ****, $P < 0.0001$).

Data availability

All data that support the findings of this study are available from the corresponding authors upon reasonable request. The raw RNA-sequencing (RNA-seq) data have been submitted to the National Center for Biotechnology Information (accession number: PRJNA777810, PRJNA779546, PRJNA779548).

Results

MIR4435-2HG within tumor cells has no biological effect on colorectal cancer cells *in vitro*

To explore the function of *MIR4435-2HG* in colorectal cancer, we analyzed 10 public datasets from The Cancer Genome Atlas (TCGA) and eligible Gene Expression Omnibus (GEO) databases (including more than 10 paired normal–tumor colorectal cancer samples), which showed that *MIR4435-2HG* was upregulated in tumor tissues compared with paired adjacent normal tissues in 7 datasets but not in the other 3 datasets (Supplementary Fig. S1A). Therefore, we performed a meta-analysis to confirm that *MIR4435-2HG* was overexpressed in colorectal cancer (**Fig. 1A**). Survival meta-analysis conducted on 8 datasets revealed no significant relationship between the expression of *MIR4435-2HG* and overall patient survival when we set the cut-off value as the Youden index or median (P50; Supplementary Fig. S1B–S1E).

Next, we detected the expression and subcellular localization of *MIR4435-2HG* in colorectal cancer cell lines (Supplementary Fig. S2A). *MIR4435-2HG* had relatively high expression in both the nucleus and cytoplasm of SW480 and RKO cells (Supplementary Fig. S2B). We knocked-out *MIR4435-2HG* through CRISPR/Cas9 in SW480 cells (Supplementary Fig. S2C) and knocked-down *MIR4435-2HG* by siRNA in SW480 and RKO cells (Supplementary Fig. S2D). Neither knockout nor knockdown of *MIR4435-2HG* in colorectal cancer cells had an effect on proliferation (Supplementary Fig. S2E and S2F), migration, or invasion (Supplementary Fig. S2G and S2H). Consistent with these findings, ectopic expression of *MIR4435-2HG* in DLD1 and HCT116 cells (Supplementary Fig. S2I) did not change their proliferation (Supplementary Fig. S2J), migration, or invasion (Supplementary Fig. S2K). RNA scope showed high expression of *MIR4435-2HG* in the tumor stroma but very low expression in colorectal cancer cells and adjacent normal epithelial cells (**Fig. 1B**), which might clarify why *MIR4435-2HG* had high expression in tumor tissues but had no biological effect within colorectal cancer cells.

Mir4435-2hg deletion promotes colorectal tumorigenesis and progression

It remains unknown whether *MIR4435-2HG* in the tumor stroma plays biological roles in colorectal cancer development. We generated *Mir4435-2hg*–deficient mice by deleting the *Mir4435-2hg* locus through CRISPR/Cas9 (Supplementary Fig. S3A–3C). Consist with a former report (35), loss of *Mir4435-2hg* led to a decline of neutrophils, monocytes, and eosinophils but not lymphoid cells (Supplementary Fig. S3D–S3F). No other obvious alterations in major organ development or dyslipidemia were observed after deleting *Mir4435-2hg* (Supplementary Fig. S4A and S4B). We then divided the mouse colitis-associated (AOM/DSS) colorectal cancer model into three cohorts, including short-term, classical term, and long-term tumor models (**Fig. 1C**), which resemble human colorectal cancer progression at the molecular level, including *Apc* mutations and β-catenin translocation (36, 37). Although the adenoma in the colorectum from the short-term tumor model was not large enough for gross observation, H&E staining showed that *Mir4435-2hg*$^{-/-}$ mice carried more colorectal adenomas and lymphoid follicles than wild-type (WT) mice (**Fig. 1D–F**). Through gross observation and H&E staining of the classical term model, we found more tumors, larger tumor sizes, and higher tumor burdens in *Mir4435-2hg*$^{-/-}$ mice than WT mice (**Fig. 1G–K**). However, neither gross observation nor H&E staining of the long-term model presented a significant difference in the tumor number or tumor size between *Mir4435-2hg*$^{-/-}$ mice and WT mice (**Fig. 1L–O**). Further histologic analysis (**Fig. 1M**) showed that all tumors from *Mir4435-2hg*$^{-/-}$ mice, but only 40% from WT mice, had penetrated through the muscularis mucosae into the submucosa (**Fig. 1P**). Another cohort of the AOM/DSS model was subjected to survival analysis (at the 30th week), and the *Mir4435-2hg*$^{-/-}$ mice exhibited worse survival (**Fig. 1Q**).

Next, *Apc*$^{Min/+}$ mice, an animal model of spontaneous intestinal adenomatous polyposis (38), were crossed with *Mir4435-2hg*$^{-/-}$ mice to mimic spontaneous tumors. Higher *Mir4435-2hg* expression was detected in intestinal tumors than in normal tissues from *Apc*$^{Min/+}$ mice (Supplementary Fig. S4C). Nevertheless, more intestinal tumors were observed in *Apc*$^{Min/+}$/*Mir4435-2hg*$^{-/-}$ mice (**Fig. 1R**; Supplementary Fig. S4D and S4E). We also found that *Apc*$^{Min/+}$/*Mir4435-2hg*$^{-/-}$ mice had worse prognosis than in *Apc*$^{Min/+}$/WT mice (**Fig. 1S**). Taken together, these data suggest that *Mir4435-2hg* depletion contributes to sporadic colorectal tumorigenesis and progression and should be considered a tumor suppressor lncRNA.

MIR4435-2HG regulates colorectal cancer development by remodeling the immune microenvironment

To demonstrate how *Mir4435-2hg* regulated colorectal cancer progression, we performed transcriptome analysis on tumor tissues from WT and *Mir4435-2hg*$^{-/-}$ AOM/DSS mice by RNA-seq. *Mir4435-2hg* deletion caused 92 genes to be significantly upregulated and 138 genes to be significantly downregulated (**Fig. 2A**), which were further validated for their representative genes by qRT-PCR (Supplementary Fig. S5A). These differentially expressed genes were mainly enriched in immune response biological processes, including inflammatory response, neutrophil chemotaxis, immune system process, antigen processing and presentation, according to Gene Ontology (GO) enrichment analysis (**Fig. 2B** and **C**).

To exclude the side effects caused by AOM/DSS-induced colitis, we also collected tumor tissues from *Apc*$^{Min/+}$/*Mir4435-2hg*$^{-/-}$ and *Apc*$^{Min/+}$/WT mice for RNA-seq analysis. Consistent with the AOM/DSS model, GO enrichment analysis of the upregulated genes showed that most genes associated with tumor immune-related biological processes, such as lymphocyte chemotaxis, cellular response to interferon-gamma, inflammatory response, and neutrophil chemotaxis (Supplementary Fig. S5C). These data further support that *Mir4435-2hg* might function as a tumor suppressor by regulating the immune microenvironment of colorectal cancer.

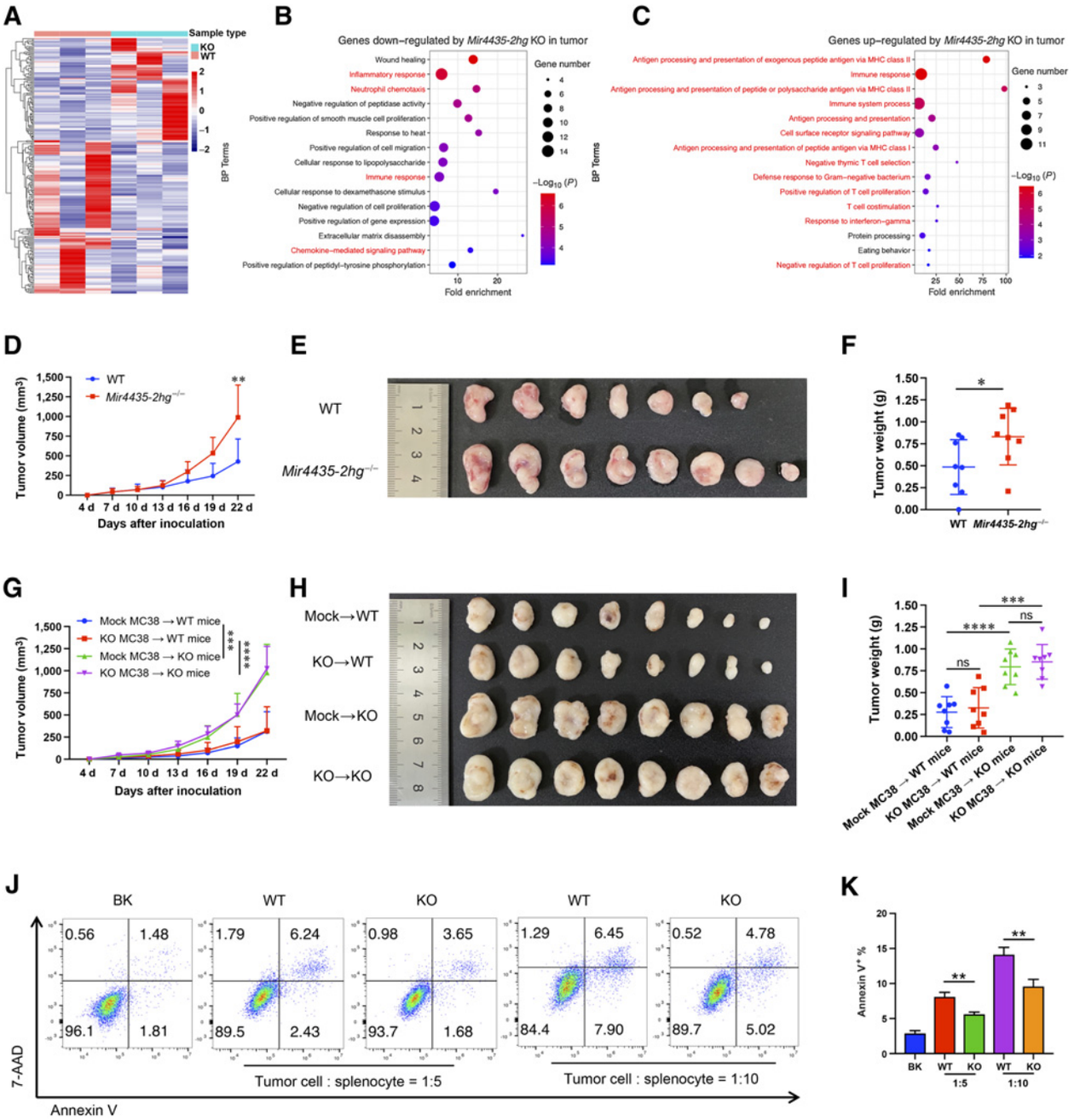

Figure 2.

MIR4435-2HG regulates colorectal cancer development by remodeling the immune microenvironment. **A,** Heat map of differentially expressed genes, determined via RNA-seq, in long-term colitis-associated (AOM/DSS) colorectal cancer tumor tissue from WT and *Mir4435-2hg*$^{-/-}$ (knockout, KO) mice, $n = 3$/group. **B,** Top downregulated biological process terms regulated by *Mir4435-2hg* depletion identified via gene ontology enrichment. **C,** Top upregulated biological process terms regulated by *Mir4435-2hg* depletion. **D,** Tumor growth curves for the subcutaneous colorectal cancer model, $n = 8$/group. 1×10^5 MC38 cells were subcutaneously inoculated to WT and *Mir4435-2hg*$^{-/-}$ (KO) mice. **E,** Tumors from WT and *Mir4435-2hg*$^{-/-}$ mice in day 22 for the model in **D**. **F,** Quantification of tumor weight for the model in **D**. **G,** Tumor growth curves for the subcutaneous colorectal cancer model, $n = 8$/group. Control (mock) or *Mir4435-2hg*$^{-/-}$ (KO) MC38 cells were subcutaneously inoculated to WT and *Mir4435-2hg*$^{-/-}$ mice. **H,** Tumors from WT and *Mir4435-2hg*$^{-/-}$ mice for the model in **G**. **I,** Quantification of tumor weight for the model in **G**. **J,** Flow cytometry analysis MC38 cell apoptosis after coculture with splenocytes from WT or *Mir4435-2hg*$^{-/-}$ mice at the indicated ratios. **K,** Quantification of proportion of Annexin V$^+$ MC38 cells, $n = 3$/group. **J** and **K,** Data are representative of three independent experiments. Data are presented as mean ± SD; statistical significance was assessed by an unpaired *t* test (ns, $P > 0.05$; *, $P < 0.05$; **, $P < 0.01$; ***, $P < 0.001$; ****, $P < 0.0001$).

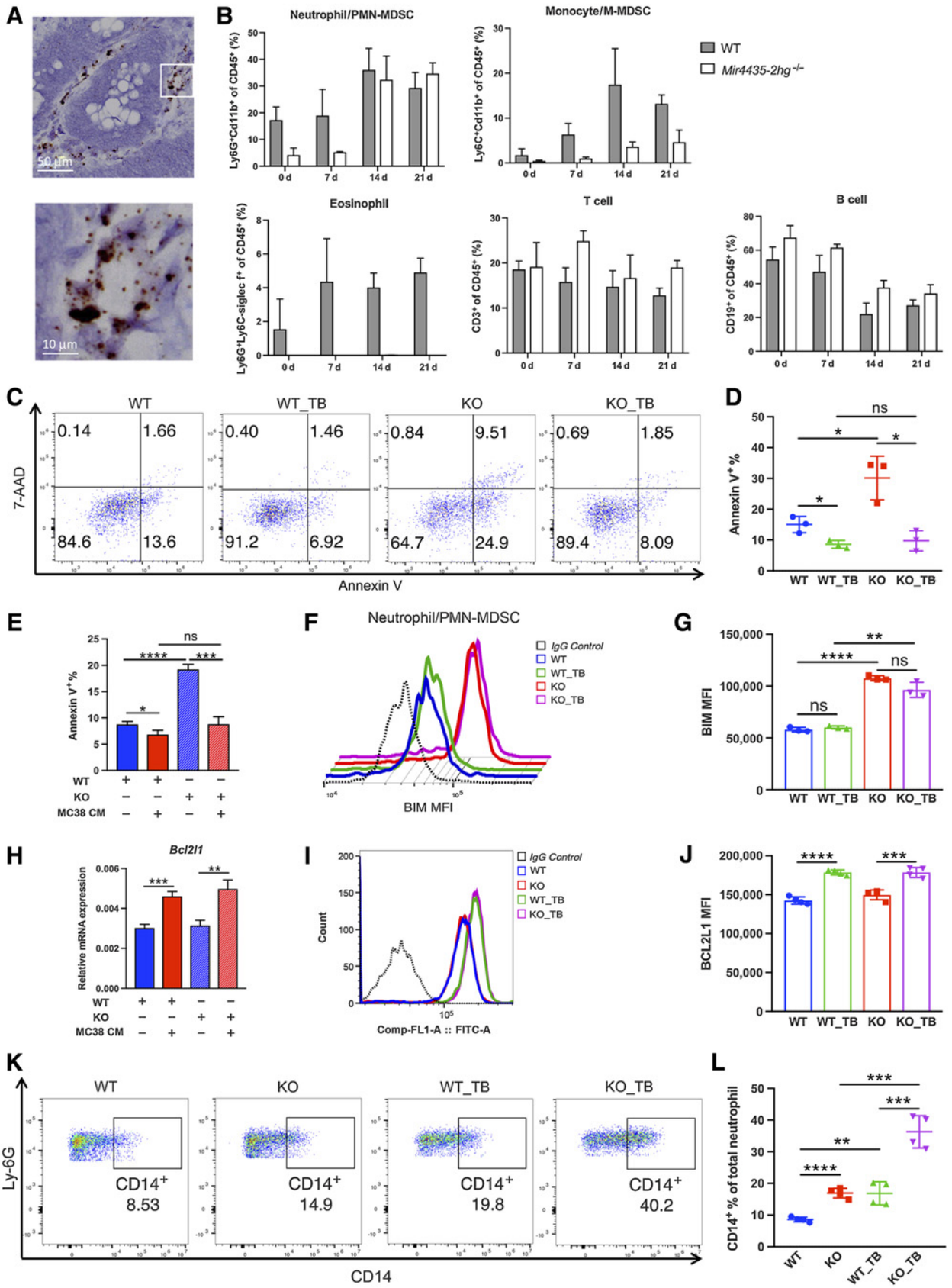
A
50 μm
10 μm
B
Neutrophil/PMN-MDSC
Ly6G+Cd11b+ of CD45+ (%)
Monocyte/M-MDSC
Ly6C+Cd11b+ of CD45+ (%)
WT
Mir4435-2hg -/-
Eosinophil
Ly6G+Ly6C-siglec f+ of CD45+ (%)
T cell
CD3+ of CD45+ (%)
B cell
CD19+ of CD45+ (%)
0 d
7 d
14 d
21 d
C
WT
WT_TB
KO
KO_TB
7-AAD
Annexin V
0.14
1.66
84.6
13.6
0.40
1.46
91.2
6.92
0.84
9.51
64.7
24.9
0.69
1.85
89.4
8.09
D
Annexin V+ %
ns
*
E
Annexin V+ %
****
***
WT
KO
MC38 CM
F
Neutrophil/PMN-MDSC
IgG Control
BIM MFI
G
BIM MFI
**
H
Bcl2l1
Relative mRNA expression
I
IgG Control
Count
Comp-FL1-A :: FITC-A
J
BCL2L1 MFI
K
Ly-6G
CD14
CD14+
8.53
14.9
19.8
40.2
L
CD14+ % of total neutrophil

To test this hypothesis, the syngeneic murine colorectal cancer cell line MC38 was subcutaneously inoculated into *Mir4435-2hg*$^{-/-}$ and WT mice. We found that tumors grew more rapidly in *Mir4435-2hg*$^{-/-}$ mice (**Fig. 2D**). The volume and weight of tumors in *Mir4435-2hg*$^{-/-}$ mice were also significantly larger than those in WT mice (**Fig. 2E** and **F**), and the tumor formation rate in *Mir4435-2hg*$^{-/-}$ mice was significantly higher than that in WT mice when the inoculated cells were diluted at different concentrations (Supplementary Fig. S5D).

To further demonstrate that *Mir4435-2hg* in the tumor stroma, but not in tumor cells, regulated colorectal cancer development, we knocked-out *Mir4435-2hg* in MC38 cells with CRISPR/Cas9 (Supplementary Fig. S5E). *Mir4435-2hg* knockout did not change their proliferation, migration, or invasion (Supplementary Fig. S5F and S5G). Overexpression of three *Mir4435-2hg* variants in MC38 and CT26 cells also had little effect on proliferation and migration (Supplementary Fig. S5H–S5J). *Mir4435-2hg* knockout MC38 and mock knockout cells were synchronously injected into *Mir4435-2hg*$^{-/-}$ and WT mice. Knocking out *Mir4435-2hg* in MC38 cells did not affect tumor proliferation in either *Mir4435-2hg*$^{-/-}$ or WT mice; however, the microenvironment of *Mir4435-2hg*$^{-/-}$ mice significantly promoted tumor growth, not only of mock but also of *Mir4435-2hg* knockout MC38 cells (**Fig. 2G**). A similar phenotype was also observed for tumor volume and weight (**Fig. 2H** and **I**). Next, we separated splenocytes from *Mir4435-2hg*$^{-/-}$ and WT mice to coculture with MC38 cells. As expected, the apoptosis of MC38 cells was greater when they were cocultured with splenocytes, but the MC38 cell apoptosis rate was decreased by the splenocytes from *Mir4435-2hg*$^{-/-}$ mice compared with WT mice (**Fig. 2J** and **K**).

We also reanalyzed survival data from TCGA and GEO databases. The ESTIMATE algorithm was used to calculate the immune score for each sample, and samples with an immune score higher than 1,000 were selected for survival analysis. In these high immune infiltrate samples, higher expression of *MIR4435-2HG* tended to associate with a better prognosis, although not statistically significant (Supplementary Fig. S6). Overall, these data indicated that *MIR4435-2HG* might play an anticancer role by remodeling the colorectal cancer immune microenvironment.

Mir4435-2hg depletion increases PMN-MDSCs in colorectal cancer

Mir4435-2hg can control the lifespan of eosinophils, neutrophils, and monocytes through allele-specific suppression of *Bim* expression (35). However, it remains unknown which type of cell in the colorectal cancer stroma expresses *Mir4435-2hg*. Therefore, we performed an RNAscope assay in human colorectal cancer tissues, which showed that *MIR4435-2HG* was mainly located in neutrophils (**Fig. 3A**). Next, we monitored the number variations of main leukocytes in peripheral blood during the growth of subcutaneous tumors. Consistent with previous reports (39), neutrophils, monocytes, and eosinophils were increased and lymphocytes were decreased in tumor-bearing mice. Monocytes and eosinophils in *Mir4435-2hg*$^{-/-}$ mice remained lower than those in WT mice, but the number of neutrophils in *Mir4435-2hg*$^{-/-}$ mice gradually reached the same frequency as that in WT mice as tumors grew (**Fig. 3B**). A similar phenotype was observed in splenocytes (Supplementary Fig. S7A).

Neutrophils in tumor-bearing mice are heterogenetic, including both classical neutrophils and PMN-MDSCs (40, 41). From our data above, we assumed that *Mir4435-2hg* could not control the lifespan of PMN-MDSCs and that the elevated neutrophils in tumor-bearing *Mir4435-2hg*$^{-/-}$ mice were mainly PMN-MDSCs. We, thus, detected the apoptosis of neutrophils in tumor-free and tumor-bearing WT and *Mir4435-2hg*$^{-/-}$ mice. Tumor-free *Mir4435-2hg*$^{-/-}$ mice had significantly more neutrophil apoptosis than the WT mice. However, in tumor-bearing mice, neutrophil apoptosis was reduced in both *Mir4435-2hg*$^{-/-}$ and WT mice, which may result from the GM-CSF produced by MC38 cells (42), and in tumor-bearing *Mir4435-2hg*$^{-/-}$ mice, neutrophil apoptosis rate was reduced to the same level as that in tumor-bearing WT mice (**Fig. 3C** and **D**). In BM-derived PMN-MDSCs, we also observed a decreased apoptosis rate after treatment with MC38 tumor cell culture medium, especially in *Mir4435-2hg*$^{-/-}$ cells (**Fig. 3E**).

Because *Mir4435-2hg* regulates neutrophil apoptosis by suppressing *Bim* expression, we detected the expression of BIM protein in neutrophils. BIM was upregulated in both tumor-free and tumor-bearing *Mir4435-2hg*$^{-/-}$ mice, and bearing tumors did not alter the expression of BIM (**Fig. 3F** and **G**; Supplementary Fig. S7B). The Bcl2 family regulates apoptosis by forming homodimers or heterodimers. Therefore, we detected alterations in all anti-apoptotic Bcl2 family members. Among them, only *Bcl2l1* in BM-derived PMN-MDSCs from either WT or *Mir4435-2hg*$^{-/-}$ mice was upregulated by stimulation with MC38 tumor cell culture medium (**Fig. 3H**), whereas *Bcl2* and *Bcl2a1a* were downregulated, and *Bcl2l2* and *Mcl1* were unaltered (Supplementary Fig. S7C). Flow cytometry also showed elevated expression of BCL2L1 in neutrophils from both WT and *Mir4435-2hg*$^{-/-}$ tumor-bearing mice (**Fig. 3I** and **J**). These results indicated that the elevated expression of BCL2L1 in PMN-MDSCs might antagonize the function of

Figure 3.

Mir4435-2hg depletion increases PMN-MDSCs. **A,** RNAscope assay showing *MIR4435-2HG* localization in tumor-infiltrating neutrophils in human colorectal cancer tissues. Representative image of five samples. Neutrophils were identified by their polymorphonuclear morphology. Brown signals represent *MIR4435-2HG*. Scale bar, 50 μm; zoomed, 10 μm. **B,** Variations in proportions of neutrophils, monocytes, eosinophils, and lymphocytes in peripheral blood of WT and *Mir4435-2hg*$^{-/-}$ (KO) mice at the indicated timepoints for subcutaneous MC38 colorectal cancer tumors, $n = 3$/group. **C,** Flow cytometry splenic neutrophil apoptosis from tumor-free WT and *Mir4435-2hg*$^{-/-}$ (KO) mice, and subcutaneous MC38 tumor-bearing wild-type (WT_TB) and *Mir4435-2hg*$^{-/-}$ (KO_TB) mice, pregated on CD11b^{+}Ly6G^{+} cells. **D,** Quantification of Annexin V^{+} neutrophils for mice in **C**, $n = 3$/group. **E,** Frequency of Annexin V^{+} neutrophils in *in vitro* cultured bone marrow (BM) cells from WT or KO mice with/without MC38 cultured medium (CM), $n = 3$/group. **F,** BIM protein expression assessed by flow cytometry in splenic neutrophils from tumor-free WT and *Mir4435-2hg*$^{-/-}$ (KO) mice, and subcutaneous MC38 tumor-bearing wild-type (WT_TB) and *Mir4435-2hg*$^{-/-}$ (KO_TB) mice. **G,** Quantification of BIM mean fluorescence intensity (MFI) from mice in (**F**), $n = 3$/group. **H,** Relative *Bcl2l1* mRNA expression in BM-derived MDSCs from WT or KO mice with/without MC38 CM, $n = 3$/group. **I,** BCL2L1 protein expression assessed by flow cytometry in splenic neutrophils from tumor-free WT and *Mir4435-2hg*$^{-/-}$ (KO) mice, and subcutaneous MC38 tumor-bearing wild-type (WT_TB) and *Mir4435-2hg*$^{-/-}$ (KO_TB) mice. **J,** Quantification of BCL2L1 MFI for mice in (I), $n = 4$/group. **K,** Representative flow cytometry of CD14^{+} neutrophils from spleen of tumor-free WT and *Mir4435-2hg* $^{-/-}$ (KO) mice, and subcutaneous MC38 tumor-bearing wild-type (WT_TB), *Mir4435-2hg*$^{-/-}$ (KO_TB) mice, pregated on CD11b^{+}Ly6G^{+} cells. **L,** Quantification of CD14^{+} neutrophils from **K**, $n = 4$ per group. **B–L,** Data are representative of three independent experiments. Data are presented as mean ± SD; statistical significance was assessed by an unpaired *t* test (ns, $P > 0.05$; *, $P < 0.05$; **, $P < 0.01$; ***, $P < 0.001$; ****, $P < 0.0001$).

the increased BIM in *Mir4435-2hg*$^{-/-}$ mice, helping the neutrophils in tumor-bearing *Mir4435-2hg*$^{-/-}$ mice recover to the same level as in WT mice and leading to a higher proportion of PMN-MDSCs.

Single-cell RNA-seq analysis (43) has identified CD14 as a marker of PMN-MDSCs for distinguishing classical neutrophils in tumor-bearing mice. In our study, a significantly higher proportion of CD14$^+$ cells was observed in splenic neutrophils from tumor-bearing *Mir4435-2hg*$^{-/-}$ mice than in those from WT mice. Even in tumor-free mice, *Mir4435-2hg*$^{-/-}$ mice also carried a higher proportion of CD14$^+$ neutrophils than WT mice (**Fig. 3K** and **L**). We also investigated several types of tumor-infiltrating immune cells within subcutaneous tumors by flow cytometry. A higher proportion of neutrophils was detected in *Mir4435-2hg*$^{-/-}$ mice than in WT mice (**Fig. 4A**). Within the neutrophil compartment, the percentage of CD14$^+$ cells reached average 85.7% in WT mice and 93.0% in *Mir4435-2hg*$^{-/-}$ mice (**Fig. 4B**), which demonstrated that tumor-infiltrating neutrophils were mostly PMN-MDSCs that were increased within the tumors of *Mir4435-2hg*$^{-/-}$ mice. In contrast, CD3$^+$ T cells

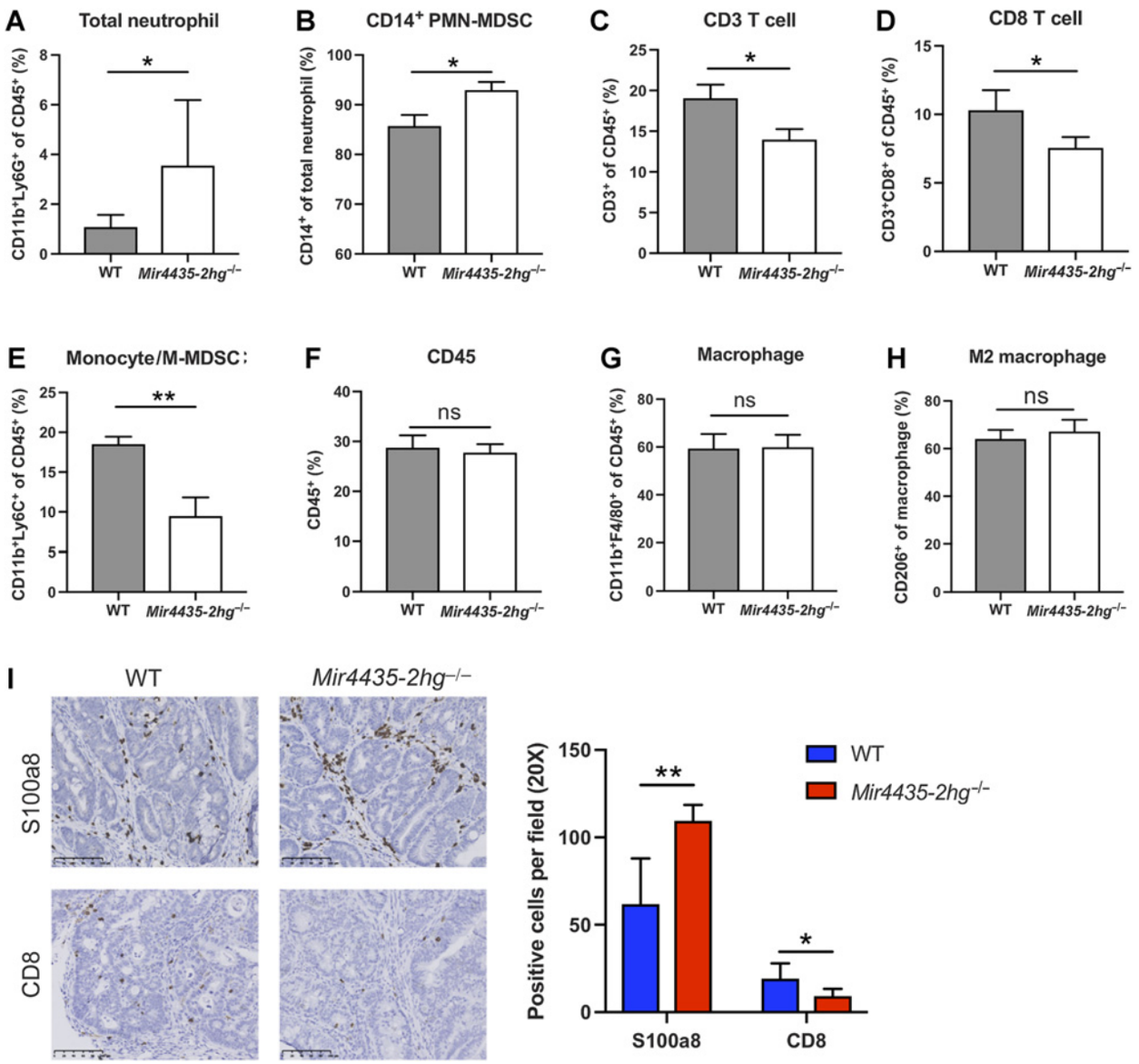

Figure 4.

Mir4435-2hg depletion leads to increased tumor-infiltrating PMN-MDSCs and decreased T cells. Flow cytometry of tumor-infiltrating total neutrophils (**A**), CD14$^+$ PMN-MDSCs (**B**), CD3$^+$ T cells (**C**), CD8$^+$ T cells (**D**), monocytes/M-MDSCs (**E**), total CD45$^+$ cells (**F**), macrophages (**G**), and M2 macrophages (**H**) in subcutaneous MC38 tumors, $n = 3$–8/group. Data are representative of three independent experiments. **I,** Left, representative IHC of tumor-infiltrating PMN-MDSCs (S100a8) and CD8$^+$ T cells (CD8) in the long-term AOM/DSS model. Scale bar, 100 μm. Right, quantification, $n = 5$/group. Data are presented as mean ± SD; statistical significance was assessed by an unpaired *t* test (ns, $P > 0.05$; *, $P < 0.05$; **, $P < 0.01$; ***, $P < 0.001$).

and $CD8^+$ T cells were decreased (**Fig. 4C** and **D**). Monocytes/M-MDSCs were also significantly decreased in *Mir4435-2hg*$^{-/-}$ mice, whereas total $CD45^+$ cells, macrophages, and M2 macrophages were unchanged (**Fig. 4E–H**). Similar results were observed in the AOM/DSS colorectal cancer model; tumor-infiltrating PMN-MDSCs were significantly increased, and $CD8^+$ T cells were decreased (**Fig. 4I**) in *Mir4435-2hg*$^{-/-}$ mice compared with WT mice by IHC. In the splenocytes/MC38 coculture system, we also observed that PMN-MDSCs were increased in the *Mir4435-2hg*$^{-/-}$ group (Supplementary Fig. S7D). These data demonstrate that loss of *Mir4435-2hg* could cause an increase in PMN-MDSCs, which contribute to an immunosuppressive environment.

Loss of *Mir4435-2hg* enhances the immunosuppressive potential of PMN-MDSCs

To investigate the biological mechanism by which *Mir4435-2hg* regulated PMN-MDSCs, we performed RNA-seq of neutrophils from BM, which showed 429 downregulated genes and 336 upregulated genes (**Fig. 5A**). GO enrichment analysis showed that the downregulated genes were enriched in mitosis-associated biological processes, including cell division, mitotic nuclear division, and regulation of mitotic centrosome separation (Supplementary Fig. S8A). Because MDSCs are considered relatively immature myeloid cells, these results might indicate a disordered process of neutrophil maturation in *Mir4435-2hg*$^{-/-}$ mice, which provides another perspective from which to understand the decline in neutrophils and the elevation of PMN-MDSCs in *Mir4435-2hg*$^{-/-}$ mice.

Most upregulated genes associated with the cholesterol biosynthetic process (**Fig. 5B**), and GSEA also showed that these genes were enriched in cholesterol homeostasis and fatty acid metabolism (**Fig. 5C** and **D**). Because accumulation of lipids is a critical regulator of the immunosuppressive function of PMN-MDSCs (44, 45), we presumed that higher lipid accumulation caused a stronger immunosuppressive effect of PMN-MDSCs in *Mir4435-2hg*$^{-/-}$ mice. Through BODIPY lipid staining, we observed an increasing trend of lipid accumulation in neutrophils from tumor-free *Mir4435-2hg*$^{-/-}$ mice, although the difference was not significant. Nevertheless, the PMN-MDSCs from the spleens of tumor-bearing *Mir4435-2hg*$^{-/-}$ mice had more lipids than those of WT mice (**Fig. 5E** and **F**). Consistent with this, *Mir4435-2hg*$^{-/-}$ mouse BM-derived PMN-MDSCs induced by CT26 and MC38 *in vitro* had more lipids than those from WT mice (**Fig. 5G**). *Mir4435-2hg*$^{-/-}$ mouse-derived PMN-MDSCs expressed higher *Arg1*, *Nos2*, *Cox2*, and ROS (**Fig. 5H–K**), which resulted in a stronger inhibitory effect on the proliferation of T cells (**Fig. 5L**). Altogether, these data illustrate that loss of *Mir4435-2hg* enhances the immunosuppressive ability of PMN-MDSCs.

Neutrophil-specific deletion of *Mir4435-2hg* promotes colorectal cancer progression

To further confirm that *Mir4435-2hg* depletion in neutrophils, but not in intestinal epithelial cells, caused the phenotypes observed in the mouse models, we generated conditional knockout *Mir4435-2hg*$^{flox/flox}$ mice and crossed them with S100a8-Cre mice or Villin-Cre mice to construct neutrophil- or intestine-specific *Mir4435-2hg* deletion mice (**Fig. 6A**; Supplementary Fig. S8B and S8C). Flow cytometry analysis of leukocytes in peripheral blood showed a decrease in neutrophils in *Mir4435-2hg*$^{flox/flox}$ S100a8-Cre mice compared to *Mir4435-2hg*$^{flox/flox}$ and *Mir4435-2hg*$^{flox/flox}$ Villin-Cre mice, and the number of eosinophils was also significantly decreased in *Mir4435-2hg*$^{flox/flox}$ S100a8-Cre mice (Supplementary Fig. S8D). The subcutaneous tumor model showed that tumors grew significantly faster in *Mir4435-2hg*$^{flox/flox}$ S100a8-Cre mice than in control mice (**Fig. 6B**), and tumor volume and weight (**Fig. 6C** and **D**) were significantly increased in neutrophil-deficient *Mir4435-2hg* mice. Consistent with the *Mir4435-2hg*$^{-/-}$ mice, we found a higher lipid accumulation in the PMN-MDSCs from tumor-bearing *Mir4435-2hg*$^{flox/flox}$ S100a8-Cre mice (**Fig. 6E**), as well as in BM-derived PMN-MDSCs induced by MC38 cultured medium *in vitro* (**Fig. 6F**).

In the AOM/DSS model, *Mir4435-2hg*$^{flox/flox}$ S100a8-Cre mice developed more and larger tumors than *Mir4435-2hg*$^{flox/flox}$ Villin-Cre and *Mir4435-2hg*$^{flox/flox}$ mice (**Fig. 6G**; Supplementary Fig. S8E). Although the tumor counts were not significantly higher in *Mir4435-2hg*$^{flox/flox}$ S100a8-Cre mice (**Fig. 6H**), the average tumor size and tumor burden (**Fig. 6I** and **J**) were significantly increased in *Mir4435-2hg*$^{flox/flox}$ S100a8-Cre mice. No obvious changes in tumor count, tumor size, or tumor burden were observed between *Mir4435-2hg*$^{flox/flox}$ Villin-Cre mice and *Mir4435-2hg*$^{flox/flox}$ mice. We also observed more tumor-infiltrating PMN-MDSCs and fewer $CD8^+$ T cells in *Mir4435-2hg*$^{flox/flox}$ S100a8-Cre mice than in *Mir4435-2hg*$^{flox/flox}$ Villin-Cre mice and *Mir4435-2hg*$^{flox/flox}$ mice (**Fig. 6K**). Overall, deletion of *Mir4435-2hg* in neutrophils/PMN-MDSCs, but not in the intestinal epithelium, promoted colorectal cancer progression.

Discussion

Here, genetically engineered mouse models demonstrated that *MIR4435-2HG* suppressed colorectal cancer initiation and progression by regulating the immunosuppressive activity of PMN-MDSCs. These findings are a significant departure from the literature, especially the colorectal cancer literature. Ouyang and colleagues (17) report *MIR4435-2HG* as a poor prognostic marker in their analysis of TCGA and two selected GEO databases. However, their analysis did not consider the high homology of *MIR4435-2HG* with *CYTOR*, which could have resulted in a false expression value for *MIR4435-2HG* that included *CYTOR* expression (TCGA anlaysis). In the GEO database, probe 232918_at is designed as a specific probe targeting *MIR4435-2HG*, whereas probe 225799_at targets both *MIR4435-2HG* and *CYTOR*. The previous study (17) used probe 225799_at to evaluate the expression value of *MIR4435-2HG*. In this study, we used the signal value of 232918_at to determine expression of *MIR4435-2HG*. We also downloaded all eligible GEO databases as of October 2017 to perform a meta-analysis, and the results revealed no significant relationship between *MIR4435-2HG* expression and overall survival. Shen and colleagues (18) investigated *MIR4435-2HG* expression in clinical colorectal cancer samples, but the primers utilized to detect *MIR4435-2HG* do not match *MIR4435-2HG* sequence. Another study reports that *MIR4435-2HG* promotes colorectal cancer proliferation and metastasis through the miR-206/YAP1 axis (19), but both the primers and the shRNA targeting *MIR4435-2HG* used also target *CYTOR*. Therefore, we believe the conclusions from these studies may not reflect the true expression of *MIR4435-2HG* and that the phenotypes observed may have been confounded by alterations in *CYTOR* expression. Other studies of *MIR4435-2HG* in other types of cancer may also need to be reexamined to verify whether off-target effects occurred. In the meanwhile, *MIR4435-2HG* might have different distribution and diverse functions in different tumor types.

In our study, we used specific CRISPR-Cas9/sgRNAs, siRNAs, and an overexpression vector to alter the expression of *MIR4435-2HG* in colorectal cancer cells, which did not affect *CYTOR* expression (Supplementary Fig. S9). Alteration of *MIR4435-2HG* did not change the

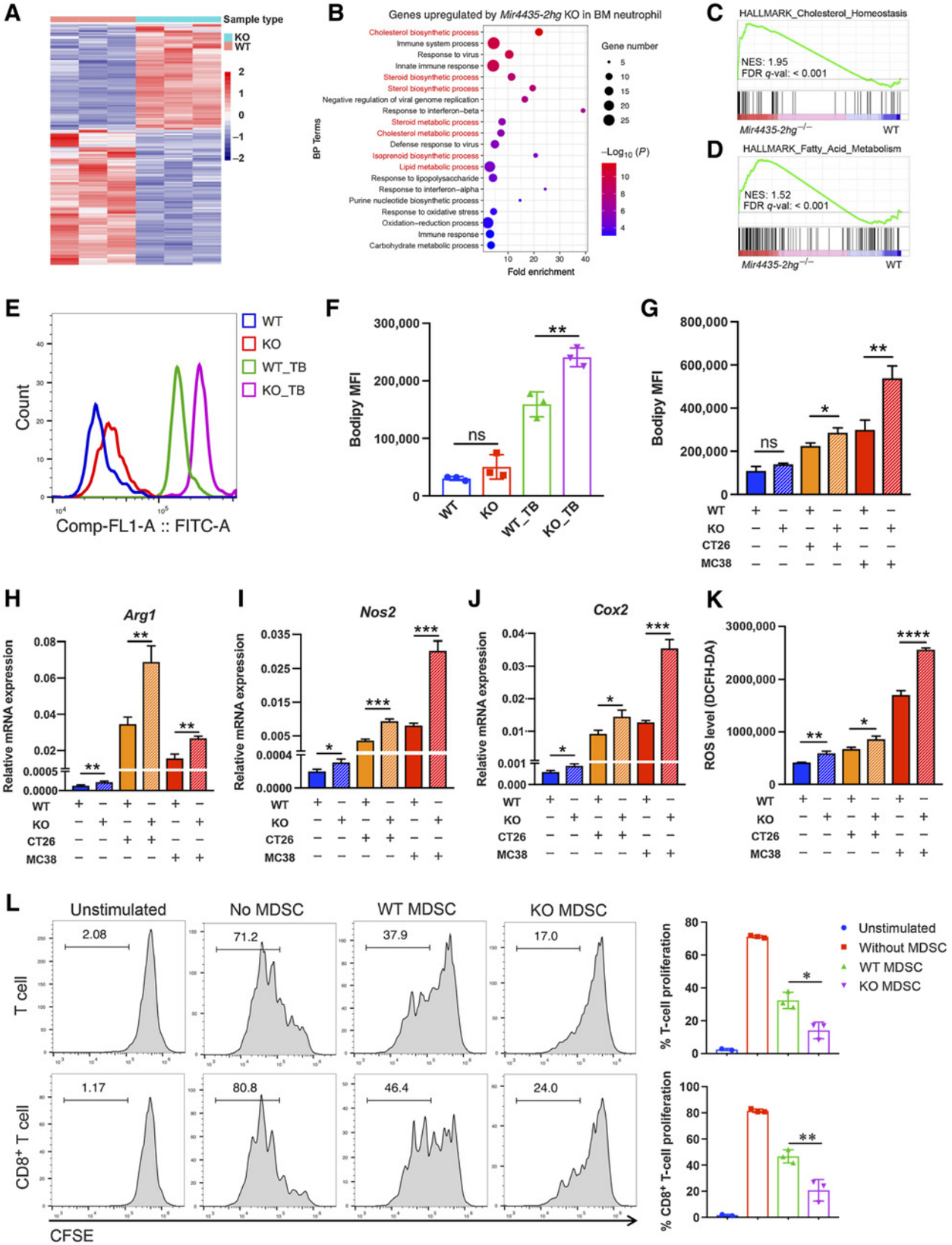
A
Sample type
KO
WT
B
Genes upregulated by Mir4435-2hg KO in BM neutrophil
Cholesterol biosynthetic process
Immune system process
Response to virus
Innate immune response
Steroid biosynthetic process
Sterol biosynthetic process
Negative regulation of viral genome replication
Response to interferon-beta
Steroid metabolic process
Cholesterol metabolic process
Defense response to virus
Isoprenoid biosynthetic process
Lipid metabolic process
Response to lipopolysaccharide
Response to interferon-alpha
Purine nucleotide biosynthetic process
Response to oxidative stress
Oxidation-reduction process
Immune response
Carbohydrate metabolic process
BP Terms
Fold enrichment
Gene number
−Log10 (P)
C
HALLMARK_Cholesterol_Homeostasis
NES: 1.95
FDR q-val: < 0.001
Mir4435-2hg−/−
WT
D
HALLMARK_Fatty_Acid_Metabolism
NES: 1.52
FDR q-val: < 0.001
Mir4435-2hg−/−
WT
E
WT
KO
WT_TB
KO_TB
Count
Comp-FL1-A :: FITC-A
F
Bodipy MFI
ns
WT
KO
WT_TB
KO_TB
G
Bodipy MFI
ns
WT
KO
CT26
MC38
H
Arg1
Relative mRNA expression
I
Nos2
Relative mRNA expression
J
Cox2
Relative mRNA expression
K
ROS level (DCFH-DA)
L
Unstimulated
No MDSC
WT MDSC
KO MDSC
T cell
CD8+ T cell
CFSE
% T-cell proliferation
% CD8+ T-cell proliferation
Unstimulated
Without MDSC
WT MDSC
KO MDSC

proliferation, migration, or invasion of human colorectal cancer cells. The same phenotypes were also observed in colorectal cancer cell lines from mice. In mice, *CYTOR* is deficient (no homologous sequence found). Because of the high level of *MIR4435-2HG* in the tumor stroma and the loss of *CYTOR* in mice, we generated *Mir4435-2hg*–deficient mice. *Mir4435-2hg*-specific depletion promoted colorectal tumorigenesis and progression in a colitis-associated colorectal cancer model, spontaneous intestinal adenomatous model, and subcutaneous tumor experiments. Although no significant change in the tumor number or tumor size was observed in the long-term colitis-associated colorectal cancer model using *Mir4435-2hg*$^{-/-}$ mice, H&E staining showed that tumors in *Mir4435-2hg*$^{-/-}$ mice exhibited higher invasion potency. The reason might be that tumor formation and proliferation reached a maximum for long-term induction, but *Mir4435-2hg* depletion still promoted colorectal cancer progression in later stages. In *Mir4435-2hg*$^{-/-}$ mice, BIM upregulation caused neutrophil apoptosis, but PMN-MDSCs with high BCL2L1 expression resisted BIM-induced apoptosis. The increased lipid accumulation in *Mir4435-2hg*$^{-/-}$ PMN-MDSCs enhanced their immunosuppressive activities. Therefore, we observed higher infiltration of PMN-MDSCs and fewer T cells in tumors from *Mir4435-2hg*$^{-/-}$ mice. In splenocyte/MC38 co-culture assays, we also observed increased PMN-MDSCs in the *Mir4435-2hg*$^{-/-}$ group, but possibly due to the low cell population and insufficient incubation time, no difference in T-cell number was observed. Nevertheless, the increased number and enhanced immunosuppressive activity of PMN-MDSCs in the *Mir4435-2hg*$^{-/-}$ group might also suppress T-cell activity, which needs to be further confirmed.

Hypercholesterolemia and dyslipidemia have previously been associated with increased baseline inflammatory responses and higher colorectal cancer incidence (46, 47). *Mir4435-2hg* depletion only led to high lipid accumulation in MDSCs, with no obvious alteration of plasma cholesterol and triglycerides (Supplementary Fig. S4B) in our mouse models. Conditional knockout of *Mir4435-2hg* in mice further confirmed that *Mir4435-2hg* depletion in neutrophils and PMN-MDSCs, but not in intestinal epithelial cells, promoted colorectal cancer development. All together, these data showed that *Mir4435-2hg* depletion regulated not only the ratio of neutrophils to PMN-MDSCs, but also the immunosuppressive activity of PMN-MDSCs, which contributed to colorectal cancer initiation and progression. Thus, we call for a rigorous reassessment of the biological characterization and clinical significance of lncRNA *MIR4435-2HG*.

Myelopoiesis is a structured process in which the common myeloid precursors in the bone marrow differentiate into mature circulating leukocytes. However, a variety of pathological conditions, such as chronic inflammation, autoimmune diseases, and cancer, can induce aberrant myelopoiesis, causing the accumulation of immature myeloid cells that diverge from the standard pathway of differentiation (48). Neutrophil differentiation involves several stages, from hematopoietic progenitor cells, common myeloid progenitors, and granulocyte-macrophage progenitors to myeloblasts, myelocytes, metamyelocytes and band forms, and then mature neutrophils (49). Under pathologic conditions, some immature myeloid cells might expand and convert to PMN-MDSCs (50). Consistent with a previous report (35), we observed a decrease in neutrophils in *Mir4435-2hg*$^{-/-}$ mice, and many differentially expressed genes regulated by *Mir4435-2hg* associated with mitosis. It needs to be further investigated whether the decrease in neutrophils in *Mir4435-2hg*$^{-/-}$ mice could increase conversion to PMN-MDSCs. Classical neutrophils, monocytes, and pathologically activated MDSCs coexist in humans and mice within tumors, and MDSCs accumulate with tumor progression (50). Mouse PMN-MDSCs are defined by the surface markers CD11b^{+}Ly6G^{+}Ly6C^{lo}, similar to classical neutrophils, which makes it difficult to distinguish PMN-MDSCs from neutrophils. Therefore, all neutrophils from tumor-bearing mice have been considered PMN-MDSCs for comparison with neutrophils from tumor-free mice in most studies. CD80, CD115, CD124, CD224, and PD-L1 are believed to be PMN-MDSC markers due to their absence on neutrophils in some experimental models (21, 51). However, these markers are not widely accepted. Veglia and colleagues propose CD14 as a specific marker of PMN-MDSCs to distinguish them from classical neutrophils using scRNA-seq in a pure population of neutrophils (43). In our study, we also observed a higher proportion of CD14^{+} cells among splenic and tumor-infiltrating neutrophils in *Mir4435-2hg*$^{-/-}$ mice, which represents a higher infiltration of PMN-MDSCs. However, whether CD14 could become the gold standard to discriminate between PMN-MDSCs and classical neutrophils needs further verification. Tumor-associated neutrophils (TAN) are another, related definition of PMN-MDSCs. These comprise a heterogeneous population that includes N1 TANs with antitumor properties and N2 TANs with suppressive functions (52). N2 TANs have been considered PMN-MDSCs (25, 53), and N1 TANs, as normally activated neutrophils, exert antitumor effects by activating unconventional T cells and exerting direct cytotoxic activity against tumors and antimicrobial activity (54). In this study, the decrease in neutrophils in *Mir4435-2hg*$^{-/-}$ and *Mir4435-2hg*$^{flox/flox}$ S100a8-Cre mice might also contributed to cancer progression, especially at early-stage disease.

Henao-Mejia and colleagues first reported that murine *Mir4435-2hg* (termed myeloid RNA regulator of Bim-induced death) could regulate *Bim* and the short myeloid cell lifespan (35). They also determined that *Mir4435-2hg* plays a vital role in viral infection (55), leukemia (56–58), and stress-induced abnormalities and clonal hematopoiesis (59). However, most studies on human

Figure 5.

Loss of *Mir4435-2hg* enhances the immunosuppressive potential of PMN-MDSCs. **A,** Heat map of differentially expressed genes, determined via RNA-seq, in BM neutrophils from naïve 8-week WT and *Mir4435-2hg*$^{-/-}$ (KO) mice, $n = 3$/group. **B,** Top upregulated biological process terms regulated by *Mir4435-2hg* depletion in BM neutrophils. GSEA for cholesterol homeostasis (**C**) and (**D**) fatty acid metabolism. Flow cytometry (**E**) and quantification of lipid accumulation (BODIPY staining; **F**) of splenic neutrophil from tumor-free WT and *Mir4435-2hg*$^{-/-}$ (KO) mice, and PMN-MDSCs from subcutaneous MC38 tumor-bearing wildtype (WT_TB) and *Mir4435-2hg*$^{-/-}$ (KO_TB) mice 20 days after MC38 cells injected, $n = 3$/group, pregated on CD11b^{+}Ly6G^{+} cells. MFI, mean fluorescence intensity. **G,** Lipid accumulation (BODIPY staining) of WT and *Mir4435-2hg*$^{-/-}$ BM-derived PMN-MDSCs with or without the stimulation of CT26 or MC38 cultured medium, $n = 3$/group. Relative *Arg1* (**H**), *Nos2* (**I**), and *Cox2* mRNA expression (**J**) in BM-derived MDSCs from cultures in **G**, assessed by qRT-PCR, $n = 3$/group. **K,** Flow cytometry of ROS (DCFH-DA probe) in BM-derived PMN-MDSCs from cultures in **G**, pregated on CD11b^{+}Ly6G^{+} cells. **L,** CFSE flow cytometry analysis of T-cell and CD8^{+} T-cell proliferation after coculture with WT or *Mir4435-2hg*$^{-/-}$ MDSCs for 72 hours, $n = 3$/group. **E–L,** Data are representative of three independent experiments. Data are presented as mean ± SD; statistical significance was assessed by an unpaired *t*-test. ns, $P > 0.05$, $^{*}P < 0.05$, $^{**}P < 0.01$, $^{***}P < 0.001$, $^{****}P < 0.0001$.

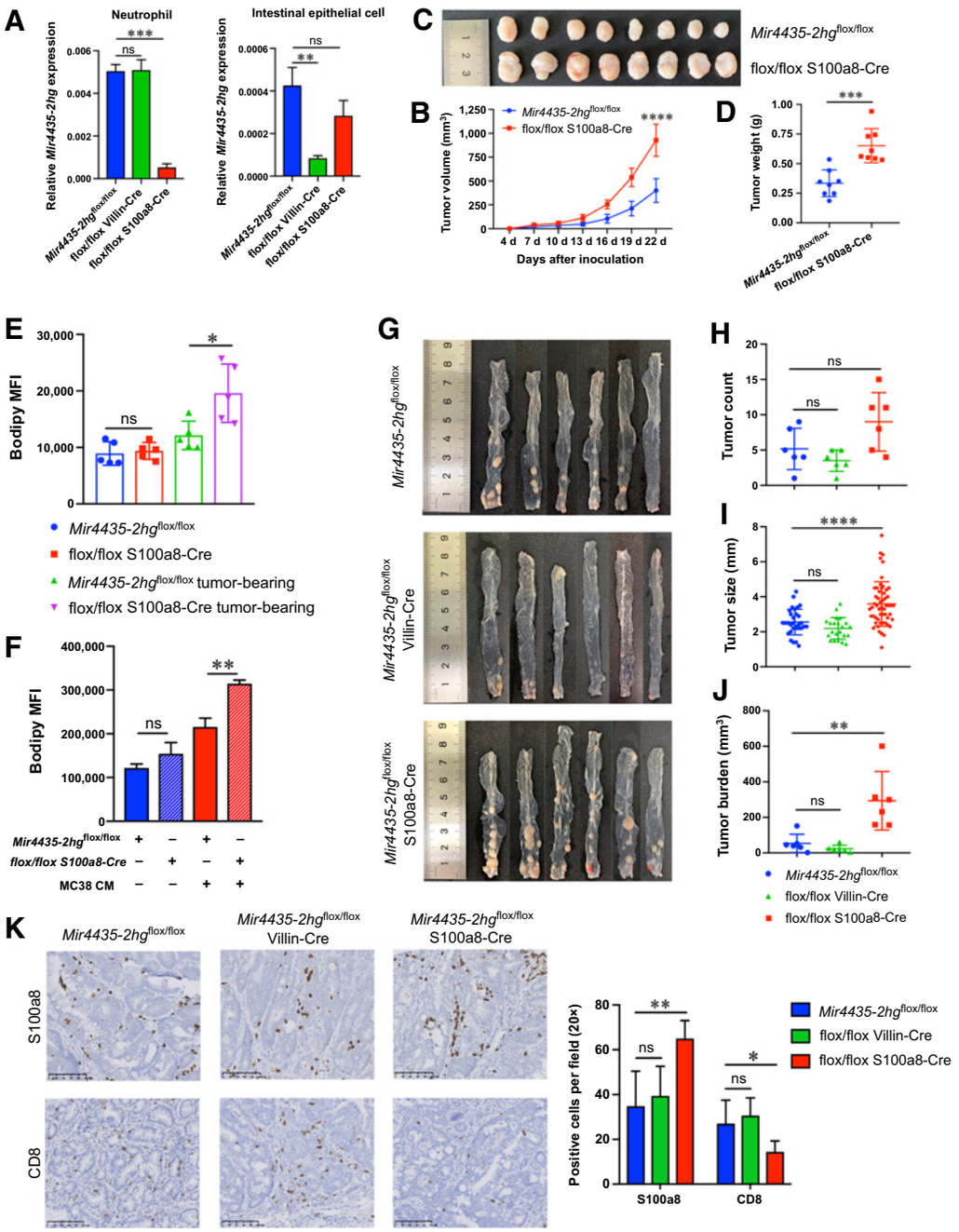

Figure 6.

Neutrophil-specific deletion of *Mir4435-2hg* promotes colorectal cancer progression. **A,** Relative *Mir4435-2hg* expression in neutrophils and intestinal epithelial cells from naïve 8-week *Mir4435-2hg*$^{flox/flox}$, *Mir4435-2hg*$^{flox/flox}$ Villin-Cre, and *Mir4435-2hg*$^{flox/flox}$ S100a8-Cre mice, n = 2–3/group. **B,** Tumor growth curves for the subcutaneous MC38 colorectal cancer model, n = 8/group, tumors were harvested at day 22. **C,** Tumors from *Mir4435-2hg*$^{flox/flox}$ and *Mir4435-2hg*$^{flox/flox}$ S100a8-Cre mice from **B**. **D,** Quantification of tumor weight from mice in **B**. **E,** Flow cytometry of lipid accumulation of splenic neutrophil from tumor-free or subcutaneous MC38 tumor-bearing *Mir4435-2hg*$^{flox/flox}$ and *Mir4435-2hg*$^{flox/flox}$ S100a8-Cre mice, n = 5/group. **F,** Lipid accumulation in the bone marrow-derived PMN-MDSCs from the indicated mice with/without MC38 culture medium (CM), n = 3/group. **G,** Gross view of colorectum from *Mir4435-2hg*$^{flox/flox}$, *Mir4435-2hg*$^{flox/flox}$ Villin-Cre, and *Mir4435-2hg*$^{flox/flox}$ S100a8-Cre mice in AOM/DSS model, n = 6/group. **H,** Quantification of tumor number from mice in (**G**); each spot represents one mouse. **I,** Quantification of tumor size from mice in **G**; each spot represents one tumor. **J,** Quantification of tumor burden from mice in **G**; each spot represents one mouse. **K,** Left, representative IHC of tumor-infiltrating PMN-MDSCs (S100a8) and CD8$^+$ T cells (CD8). Scale bar, 100 μm. Right, quantification, n = 5/group. (**A**, **E**, and **F**) Data are representative of three independent experiments. Data are presented as mean ± SD; statistical significance was assessed by an unpaired t test (ns, $P > 0.05$; *, $P < 0.05$; **, $P < 0.01$; ***, $P < 0.001$; ****, $P < 0.0001$).

MIR4435-2HG have focused on cancer biology. Reports analyzing TCGA data for colorectal cancer (60), hepatocellular carcinoma (61), and pan-cancer (62) have revealed that *MIR4435-2HG* associates with glycolysis and immune infiltration. Together, these data and our data suggest that these correlations should be attributed to the high expression of *MIR4435-2HG* in immune cells. High immune infiltration leads to a high expression of *MIR4435-2HG* in tumor tissues. *MIR4435-2HG* could activate oxidative phosphorylation in myeloid dendritic cells (DCs) from HIV-1 elite controllers by regulating epigenetic modifications and facilitating the transcription of Regulatory-Associated Protein of MTOR Complex 1 (*RPTOR*) (63). This emerging evidence implies that *MIR4435-2HG* could also control other immune cells besides neutrophils and PMN-MDSCs, such as DCs and eosinophils, to regulate tumor progression. According to our data, *Mir4435-2hg* depletion almost resulted in the absence of eosinophils. Higher eosinophil infiltration is reported to associate with better prognosis in colorectal cancer (64). Therefore, we did not exclude the tumor-suppressive roles of eosinophils, which are worth further exploring.

In conclusion, our study demonstrates the unexpected role of *MIR4435-2HG* using multiple mouse models. It functioned as a tumor suppressor in the tumor stroma by remodeling the immune microenvironment rather than as an oncogene in tumor cells. The deficiency of *MIR4435-2HG* increased tumor-infiltrating PMN-MDSCs and enhanced their immunosuppressive potential to promote colorectal cancer development, further illustrating mechanisms behind the pathogenesis of colorectal cancer and providing a potential antitumor immunotherapy target.

Authors' Disclosures

No disclosures were reported.

Authors' Contributions

H. Yu: Data curation, software, formal analysis, validation, investigation, visualization, methodology, writing–original draft, writing–review and editing. **C. Chen:** Data curation, software, formal analysis, visualization, methodology, writing–review and editing. **F. Han:** Data curation, software, formal analysis, methodology. **J. Tang:** Formal analysis, visualization, methodology. **M. Deng:** Investigation. **Y. Niu:** Investigation, writing–original draft. **M. Lai:** Conceptualization, resources, data curation, supervision, funding acquisition, project administration. **H. Zhang:** Conceptualization, resources, data curation, supervision, funding acquisition, writing–original draft, project administration, writing–review and editing.

Acknowledgments

This work is supported by the National Natural Science Foundation of China (81871937, 81672730, 91859204, 82072629, 82173223), the Natural Science Foundation of Zhejiang Province (LZ21H160001) and CAMS Innovation Fund for Medical Sciences (CIFMS, 2019-I2M-5-044). We are grateful to Rongpan Bai, Zhejiang University School of Medicine, for providing $APC^{min/+}$ mice. We thank Ms. Xueping Zhou in the Laboratory Animal Center of Zhejiang University for technical assistance on breeding and management of mice and Ms. Qiong Huang for the technical support by the Core Facilities, Zhejiang University School of Medicine.

The costs of publication of this article were defrayed in part by the payment of page charges. This article must therefore be hereby marked *advertisement* in accordance with 18 U.S.C. Section 1734 solely to indicate this fact.

Note

Supplementary data for this article are available at Cancer Immunology Research Online (http://cancerimmunolres.aacrjournals.org/).

Received November 29, 2021; revised March 31, 2022; accepted July 15, 2022; published first July 20, 2022.

References

1. Mercer TR, Dinger ME, Mattick JS. Long non-coding RNAs: insights into functions. Nat Rev Genet 2009;10:155–9.
2. Bhan A, Soleimani M, Mandal SS. Long Noncoding RNA and Cancer: A new paradigm. Cancer Res 2017;77:3965–81.
3. Zhou L, Zhu Y, Sun D, Zhang Q. Emerging roles of long non-coding RNAs in the tumor microenvironment. Int J Biol Sci 2020;16:2094–103.
4. Siegel RL, Miller KD, Fuchs HE, Jemal A. Cancer statistics, 2021. CA Cancer J Clin 2021;71:7–33.
5. Kong J, Sun W, Li C, Wan L, Wang S, Wu Y, et al. Long non-coding RNA LINC01133 inhibits epithelial–mesenchymal transition and metastasis in colorectal cancer by interacting with SRSF6. Cancer Lett 2016; 380:476–84.
6. Wang X, Yu H, Sun W, Kong J, Zhang L, Tang J, et al. The long non-coding RNA CYTOR drives colorectal cancer progression by interacting with NCL and Sam68. Mol Cancer 2018;17:110.
7. Nötzold L, Frank L, Gandhi M, Polycarpou-Schwarz M, Groß M, Gunkel M, et al. The long non-coding RNA LINC00152 is essential for cell cycle progression through mitosis in HeLa cells. Sci Rep 2017;7:2265.
8. Yang M, He X, Huang X, Wang J, He Y, Wei L. LncRNA MIR4435-2HG-mediated upregulation of TGF-β1 promotes migration and proliferation of nonsmall cell lung cancer cells. Environ Toxicol 2020;35:582–90.
9. Qian H, Chen L, Huang J, Wang X, Ma S, Cui F, et al. The lncRNA MIR4435-2HG promotes lung cancer progression by activating β-catenin signalling. J Mol Med Berl Ger 2018;96:753–64.
10. Shen X, Ding Y, Lu F, Yuan H, Luan W. Long noncoding RNA MIR4435-2HG promotes hepatocellular carcinoma proliferation and metastasis through the miR-22–3p/YWHAZ axis. Am J Transl Res 2020;12:6381–94.
11. Kong Q, Liang C, Jin Y, Pan Y, Tong D, Kong Q, et al. The lncRNA MIR4435-2HG is upregulated in hepatocellular carcinoma and promotes cancer cell proliferation by upregulating miRNA-487a. Cell Mol Biol Lett 2019;24:26.
12. Wang H, Wu M, Lu Y, He K, Cai X, Yu X, et al. LncRNA MIR4435-2HG targets desmoplakin and promotes growth and metastasis of gastric cancer by activating Wnt/β-catenin signaling. Aging 2019;11:6657–73.
13. Chen D, Tang P, Wang Y, Wan F, Long J, Zhou J, et al. Downregulation of long non-coding RNA MR4435-2HG suppresses breast cancer progression via the Wnt/β-catenin signaling pathway. Oncol Lett 2021;21:373.
14. Deng L, Chi Y, Liu L, Huang N, Wang L, Wu J. LINC00978 predicts poor prognosis in breast cancer patients. Sci Rep 2016;6:37936.
15. Xing P, Wang Y, Zhang L, Ma C, Lu J. Knockdown of lncRNA MIR4435-2HG and ST8SIA1 expression inhibits the proliferation, invasion and migration of prostate cancer cells in vitro and in vivo by blocking the activation of the FAK/AKT/β-catenin signaling pathway. Int J Mol Med 2021;47:93.
16. Zhang H, Meng H, Huang X, Tong W, Liang X, Li J, et al. lncRNA MIR4435-2HG promotes cancer cell migration and invasion in prostate carcinoma by upregulating TGF-β1. Oncol Lett 2019;18:4016–21.
17. Ouyang W, Ren L, Liu G, Chi X, Wei H. LncRNA MIR4435-2HG predicts poor prognosis in patients with colorectal cancer. PeerJ 2019;7:e6683.
18. Shen M-Y, Zhou G-R, Zhang Z-Y. LncRNA MIR4435-2HG contributes into colorectal cancer development and predicts poor prognosis. Eur Rev Med Pharmacol Sci 2020;24:1771–7.
19. Dong X, Yang Z, Yang H, Li D, Qiu X. Long Non-coding RNA MIR4435-2HG Promotes Colorectal Cancer Proliferation and Metastasis Through miR-206/YAP1 Axis. Front Oncol 2020;10:160.
20. Gabrilovich DI, Bronte V, Chen S-H, Colombo MP, Ochoa A, Ostrand-Rosenberg S, et al. The terminology issue for myeloid-derived suppressor cells. Cancer Res 2007;67:425.
21. Youn J-I, Nagaraj S, Collazo M, Gabrilovich DI. Subsets of Myeloid-Derived Suppressor Cells in Tumor-Bearing Mice. J Immunol 2008;181:5791–802.

22. Youn J-I, Kumar V, Collazo M, Nefedova Y, Condamine T, Cheng P, et al. Epigenetic silencing of retinoblastoma gene regulates pathologic differentiation of myeloid cells in cancer. Nat Immunol 2013;14:211–20.
23. Messmer MN, Netherby CS, Banik D, Abrams SI. Tumor-induced myeloid dysfunction and its implications for cancer immunotherapy. Cancer Immunol Immunother 2015;64:1–13.
24. Raber P, Ochoa AC, Rodríguez PC. Metabolism of L-Arginine by Myeloid-Derived Suppressor Cells in Cancer: Mechanisms of T cell suppression and Therapeutic Perspectives. Immunol Invest 2012;41:614–34.
25. Raber PL, Thevenot P, Sierra R, Wyczechowska D, Halle D, Ramirez ME, et al. Subpopulations of myeloid-derived suppressor cells impair T cell responses through independent nitric oxide-related pathways. Int J Cancer 2014;134:2853–64.
26. Gabrilovich DI, Nagaraj S. Myeloid-derived suppressor cells as regulators of the immune system. Nat Rev Immunol 2009;9:162–74.
27. Limagne E, Euvrard R, Thibaudin M, Rébé C, Derangère V, Chevriaux A, et al. Accumulation of MDSC and Th17 cells in patients with metastatic colorectal cancer predicts the efficacy of a FOLFOX-bevacizumab drug treatment regimen. Cancer Res 2016;76:5241–52.
28. OuYang L-Y, Wu X-J, Ye S-B, Zhang R-X, Li Z-L, Liao W, et al. Tumor-induced myeloid-derived suppressor cells promote tumor progression through oxidative metabolism in human colorectal cancer. J Transl Med 2015;13:47.
29. Zheng Y, Tian X, Wang T, Xia X, Cao F, Tian J, et al. Long noncoding RNA Pvt1 regulates the immunosuppression activity of granulocytic myeloid-derived suppressor cells in tumor-bearing mice. Mol Cancer 2019;18:61.
30. Gao Y, Sun W, Shang W, Li Y, Zhang D, Wang T, et al. Lnc-C/EBPβ negatively regulates the suppressive function of myeloid-derived suppressor cells. Cancer Immunol Res 2018;6:1352–63.
31. Gao Y, Wang T, Li Y, Zhang Y, Yang R. Lnc-chop promotes immunosuppressive function of Myeloid-derived suppressor cells in tumor and inflammatory environments. J Immunol 2018;200:2603–14.
32. Han F, Zhang L, Chen C, Wang Y, Zhang Y, Qian L, et al. GLTSCR1 negatively regulates BRD4-dependent transcription elongation and inhibits CRC metastasis. Adv Sci 2019;6:1901114.
33. Yoshihara K, Shahmoradgoli M, Martínez E, Vegesna R, Kim H, Torres-Garcia W, et al. Inferring tumour purity and stromal and immune cell admixture from expression data. Nat Commun 2013;4:2612.
34. Trapnell C, Hendrickson DG, Sauvageau M, Goff L, Rinn JL, Pachter L. Differential analysis of gene regulation at transcript resolution with RNA-seq. Nat Biotechnol 2013;31:46–53.
35. Kotzin JJ, Spencer SP, McCright SJ, Kumar DBU, Collet MA, Mowel WK, et al. The long non-coding RNA Morrbid regulates Bim and short-lived myeloid cell lifespan. Nature 2016;537:239–43.
36. Neufert C, Becker C, Neurath MF. An inducible mouse model of colon carcinogenesis for the analysis of sporadic and inflammation-driven tumor progression. Nat Protoc 2007;2:1998–2004.
37. Robertis MD, Massi E, Poeta ML, Carotti S, Morini S, Cecchetelli L, et al. The AOM/DSS murine model for the study of colon carcinogenesis: From pathways to diagnosis and therapy studies. J Carcinog 2011;10:9.
38. Su LK, Kinzler KW, Vogelstein B, Preisinger AC, Moser AR, Luongo C, et al. Multiple intestinal neoplasia caused by a mutation in the murine homolog of the APC gene. Science 1992;256:668–70.
39. Kuwabara WMT, Andrade-Silva J, Pereira JNB, Scialfa JH, Cipolla-Neto J. Neutrophil activation causes tumor regression in Walker 256 tumor-bearing rats. Sci Rep 2019;9:16524.
40. Mishalian I, Granot Z, Fridlender ZG. The diversity of circulating neutrophils in cancer. Immunobiology 2017;222:82–8.
41. Ng LG, Ostuni R, Hidalgo A. Heterogeneity of neutrophils. Nat Rev Immunol 2019;19:255–65.
42. Urdinguio RG, Fernandez AF, Moncada-Pazos A, Huidobro C, Rodriguez RM, Ferrero C, et al. Immune-dependent and independent antitumor activity of GM-CSF aberrantly expressed by mouse and human colorectal tumors. Cancer Res 2013;73:395–405.
43. Veglia F, Hashimoto A, Dweep H, Sanseviero E, De Leo A, Tcyganov E, et al. Analysis of classical neutrophils and polymorphonuclear myeloid-derived suppressor cells in cancer patients and tumor-bearing mice. J Exp Med 2021;218: e20201803.
44. Veglia F, Tyurin VA, Blasi M, De Leo A, Kossenkov AV, Donthireddy L, et al. Fatty acid transport protein 2 reprograms neutrophils in cancer. Nature 2019; 569:73–8.
45. Hicks KC, Tyurina YY, Kagan VE, Gabrilovich DI. Myeloid Cell–Derived Oxidized Lipids and Regulation of the Tumor Microenvironment. Cancer Res 2022;82:187–94.
46. Tall AR, Yvan-Charvet L. Cholesterol, inflammation and innate immunity. Nat Rev Immunol 2015;15:104–16.
47. Cowey S, Hardy RW. The Metabolic Syndrome. Am J Pathol 2006;169: 1505–22.
48. Bronte V, Brandau S, Chen S-H, Colombo MP, Frey AB, Greten TF, et al. Recommendations for myeloid-derived suppressor cell nomenclature and characterization standards. Nat Commun 2016;7:12150.
49. Evrard M, Kwok IWH, Chong SZ, Teng KWW, Becht E, Chen J, et al. Developmental analysis of bone marrow neutrophils reveals populations specialized in expansion, trafficking, and effector functions. Immunity 2018; 48:364–79.
50. Veglia F, Perego M, Gabrilovich D. Myeloid-derived suppressor cells coming of age. Nat Immunol 2018;19:108–19.
51. Youn J-I, Collazo M, Shalova IN, Biswas SK, Gabrilovich DI. Characterization of the nature of granulocytic myeloid-derived suppressor cells in tumor-bearing mice. J Leukoc Biol 2012;91:167–81.
52. Fridlender ZG, Sun J, Kim S, Kapoor V, Cheng G, Ling L, et al. Polarization of tumor-associated neutrophil phenotype by TGF-beta: "N1" versus "N2" TAN. Cancer Cell 2009;16:183–94.
53. Cimen Bozkus C, Elzey BD, Crist SA, Ellies LG, Ratliff TL. Expression of cationic amino acid transporter 2 is required for Myeloid-derived suppressor Cell-mediated control of T cell immunity. J Immunol 2015;195:5237–50.
54. Jaillon S, Ponzetta A, Di Mitri D, Santoni A, Bonecchi R, Mantovani A. Neutrophil diversity and plasticity in tumour progression and therapy. Nat Rev Cancer 2020;20:485–503.
55. Kotzin JJ, Iseka F, Wright J, Basavappa MG, Clark ML, Ali M-A, et al. The long noncoding RNA Morrbid regulates CD8 T cells in response to viral infection. Proc Natl Acad Sci U S A 2019;116:11916–25.
56. Cai Z, Aguilera F, Ramdas B, Daulatabad SV, Srivastava R, Kotzin JJ, et al. Targeting Bim via a lncRNA morrbid regulates the survival of preleukemic and leukemic cells. Cell Rep 2020;31:107816.
57. Cai Z, Lu X, Zhang C, Nelanuthala S, Aguilera F, Hadley A, et al. Hyperglycemia cooperates with Tet2 heterozygosity to induce leukemia driven by proinflammatory cytokine-induced lncRNA Morrbid. J Clin Invest 2021;131:140707.
58. Cai Z, Zhang C, Kotzin JJ, Williams A, Henao-Mejia J, Kapur R. Role of lncRNA Morrbid in PTPN11(Shp2)E76K-driven juvenile myelomonocytic leukemia. Blood Adv 2020;4:3246–51.
59. Cai Z, Kotzin JJ, Ramdas B, Chen S, Nelanuthala S, Palam LR, et al. Inhibition of inflammatory signaling in Tet2 mutant preleukemic cells mitigates Stress-induced abnormalities and clonal hematopoiesis. Cell Stem Cell 2018;23: 833–49.
60. Chen J, Song Y, Li M, Zhang Y, Lin T, Sun J, et al. Comprehensive analysis of ceRNA networks reveals prognostic lncRNAs related to immune infiltration in colorectal cancer. BMC Cancer 2021;21:255.
61. Bai Y, Lin H, Chen J, Wu Y, Yu S. Identification of prognostic Glycolysis-related lncRNA signature in tumor immune microenvironment of hepatocellular carcinoma. Front Mol Biosci 2021;8:645084.
62. Ho K-H, Huang T-W, Shih C-M, Lee Y-T, Liu A-J, Chen P-H, et al. Glycolysis-associated lncRNAs identify a subgroup of cancer patients with poor prognoses and a high-infiltration immune microenvironment. BMC Med 2021; 19:59.
63. Hartana CA, Rassadkina Y, Gao C, Martin-Gayo E, Walker BD, Lichterfeld M, et al. Long noncoding RNA MIR4435-2HG enhances metabolic function of myeloid dendritic cells from HIV-1 elite controllers. J Clin Invest 2021;131: e146136.
64. Prizment AE, Vierkant RA, Smyrk TC, Tillmans LS, Lee JJ, Sriramarao P, et al. Tumor eosinophil infiltration and improved survival of colorectal cancer patients: Iowa Women's Health Study. Mod Pathol 2016;29:516–27.